Numerical simulations of particle sedimentation using the immersed boundary method[☆]

Sudeshna Ghosh[a], John M. Stockie[a,*]

[a]*Department of Mathematics, Simon Fraser University, 8888 University Drive, Burnaby, BC, V5A 1S6, Canada*

Abstract

We study the settling of solid particles within a viscous incompressible fluid contained in a two-dimensional channel, where the mass density of the particles is slightly greater than that of the fluid. The fluid-structure interaction problem is simulated numerically using the immersed boundary method, with an added mass term that is incorporated using a Boussinesq approximation. Simulations are performed with a single circular particle, and also with two particles in various initial configurations. The terminal settling velocities for the particles correspond closely with both theoretical and experimental results, and the single-particle dynamics reproduce expected behavior qualitatively. The two-particle simulations exhibit drafting-kissing-tumbling dynamics that is similar to what is observed in other experimental and numerical studies.

Keywords: immersed boundary method, particle suspension, sedimentation, settling velocity, fluid-structure interaction
2010 MSC: 76T20, 65M08

1. Introduction.

Particulate flows involve a dynamically evolving fluid that interacts with solid suspended particles, and arise in a wide range of applications in natural and industrial processes [9]. We are particularly interested in the gravitational settling or sedimentation problem, in which the suspended solid particles have large enough mass that they settle under their own weight. Sedimentation is observed in many applications, including flow of pollutants in rivers and the atmosphere, tea leaves settling to the bottom of a teacup, industrial crystal precipitation, mineral ore processing, and hail formation in thunderclouds, to name just a few.

There is an extensive literature on experimental, theoretical and computational studies of particulate flows involving sedimentation. We make no attempt here to perform a comprehensive review, but will rather highlight a few of the more important results. Experimental studies of sedimentation have had a long history including the earlier work of Richardson and Zaki [40] and extending to more recent years [15, 17, 27, 28]. Many analytical and approximate solutions have been developed to explain the behavior of settling suspensions, especially in the dilute limit where there are only a small number of particles. Back in 1851, Stokes [43] derived an analytical solution for a single particle settling within an unbounded fluid, and many other authors have since extended these results to other more practical sedimentation problems [6, 12, 21, 47]. More recently, many numerical approaches have been applied to simulate settling particles, including the finite element method [16, 19, 26, 33], lattice-Boltzmann method [13, 30, 39], and boundary element method [24, 36]. The underlying feature of these numerical methods is that the fluid flow is governed by the Navier-Stokes equations whereas the particles are governed by Newton's equations of motion. The hydrodynamic

[☆]This work was supported by grants from the Natural Sciences and Engineering Research Council of Canada and the Mprime Network of Centres of Excellence.

[*]corresponding author
Email addresses: sga33@sfu.ca (Sudeshna Ghosh), stockie@math.sfu.ca (John M. Stockie)
URL: http://www.math.sfu.ca/~stockie (John M. Stockie)

forces between the particle and fluid are obtained from the solution of this coupled system, which typically requires either complex interfacial matching conditions at the fluid-particle interface, or else some form of dynamic boundary-fitted meshing. In any case, these methods tend to be complex and extremely CPU-intensive, especially for three-dimensional flows.

One numerical approach that has proven to be especially effective for solving complex fluid-structure interaction problems involving dynamic moving structures is the *immersed boundary* (or IB) method. This approach has been used extensively to simulate deformable structures arising in problems in biofluid mechanics [35]. Wang and Layton [48] have recently used the IB method to simulate sedimentation of multiple rigid 1D fibers suspended in a viscous incompressible fluid, and several other authors have applied the the IB approach to solve related sedimentation problems [7, 13, 25, 46, 49].

The IB method is a mixed Eulerian-Lagrangian approach, in which the fluid equations are solved on an equally-spaced rectangular mesh, while the moving solid boundaries are approximated at a set of points that moves relative to the underlying fluid grid. In the original IB method, the effect of these immersed boundaries is represented as a singular force that is computed from the IB configuration and which is then spread onto fluid grid points by means of a regularized delta function. The added mass due to a sedimenting particle can also be distributed onto the fluid in a similar manner. With the exception of the papers by Wang and Layton [48] and Hopkins and Fauci [25], the other authors mentioned above have employed a modification of this IB approach known as the "direct forcing IB method," wherein the force is an artificial quantity that is calculated directly from the governing equations so as to satisfy the velocity boundary conditions exactly on the immersed boundary (see [32] for more details).

Our aim in this paper is to apply the original IB method to solving sedimentation problems, rather than the direct forcing approach. We restrict ourselves to a two-dimensional geometry, in which one or two particles with a circular cross-section settle under the influence of gravity within a rectangular channel that has vertical bounding walls. Although the IB approach has been applied to solve certain sedimentation problems, there has not yet been an extensive comparison to other results in the literature. Our primary aim is therefore to perform such a comparison to a number of experimental [44, 50], theoretical [14, 45], and numerical [16] studies, in order to ascertain the validity of the IB approach in simulating sedimentation problems. Although we focus here on solid particles, the long-term goal of our work is to develop a numerical framework that can be used to investigate the settling of highly deformable particles.

We begin in Section 2 by describing the IB method and defining the forces used to simulate the presence of both settling particles and channel walls. Section 3 contains a review of previous analytical and experimental results on the settling velocity for a single particle in both unbounded and wall-bounded domains. We then perform a series of numerical simulations of sedimentation at small to moderate Reynolds numbers, and report the results in Sections 4 and 5. Most of the results appearing in this article are contained in the PhD thesis of the first author [18].

2. Immersed boundary method.

The immersed boundary method is both a mathematical formulation and a numerical scheme. We begin in this section by describing the model equations that underlie the IB formulation for fluid-structure interaction. Following that, we discretize the equations and describe the numerical algorithm used to determine an approximate solution. Finally, we provide details on the specification of the discrete IB force density representing the channel walls and sedimenting particles.

2.1. Model formulation.

In this section we describe a two-dimensional IB model that is capable of capturing solid (and potentially deformable) elastic bodies with general shape and that move within a surrounding incompressible, Newtonian fluid under the action of gravitational force. The details of the IB force density used to handle a solid circular object in the presence of two parallel bounding walls are left for section 2.3. All variables and parameters in this paper are stated in CGS units, unless otherwise indicated.

Suppose that a moving elastic solid body Γ is contained within a fluid domain Ω as pictured in Figure 1. In general, Γ may consist of several disconnected components, $\Gamma = \bigcup_i \Gamma_i$, where each Γ_i can be a one-

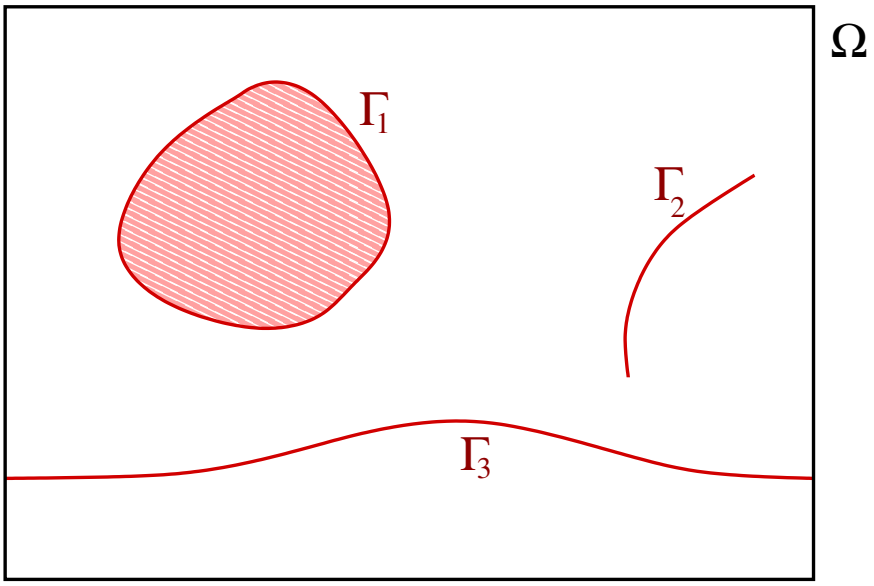

Figure 1: A general immersed boundary configuration $\Gamma = \bigcup_{i=1}^{3} \Gamma_i$ consisting of several disconnected components immersed within a doubly-periodic fluid domain Ω.

dimensional elastic membrane (parameterized by a single real parameter s) or an elastic solid region (whose specification requires two parameters, r and s). We denote the location or "configuration" of the immersed boundary by $\boldsymbol{X}(\boldsymbol{q},t)$ [cm], where $\boldsymbol{q}$ is a dimensionless IB parameterization that is used to represent either a scalar s or a vector (r,s), depending on the context. For simplicity, we assume that $\Omega = [0,L_x] \times [0,L_y]$ is rectangular in shape and that periodic boundary conditions are applied in both the x- and y-directions.

The effect of the elastic body on the fluid is to impose a force $\boldsymbol{f}_{IB}$ [g/cm^2 s^2] onto the adjacent fluid particle at location $\boldsymbol{x} = \boldsymbol{X}(\boldsymbol{q},t)$, which is incorporated into the incompressible Navier-Stokes equations as follows:

$$\rho \frac{\partial \boldsymbol{u}}{\partial t} + \rho \boldsymbol{u} \cdot \nabla \boldsymbol{u} = \mu \nabla^2 \boldsymbol{u} - \nabla p + \boldsymbol{f}_{IB}, \tag{1}$$

$$\nabla \cdot \boldsymbol{u} = 0. \tag{2}$$

Here, $\boldsymbol{u}(\boldsymbol{x},t)$ is the fluid velocity [cm/s], $p(\boldsymbol{x},t)$ is the pressure [g/cm s^2], $\boldsymbol{x} = (x,y)$ are the Eulerian coordinates [cm] for the fluid domain Ω, ρ is density [g/cm^3] and μ is dynamic viscosity [g/cm s]. The IB forcing term in the momentum equations (1) is represented by a force density $\boldsymbol{F}_{IB}(\boldsymbol{q},t)$ [g/s^2] that is spread onto the surrounding fluid by means of a delta-function convolution

$$\boldsymbol{f}_{IB}(\boldsymbol{x},t) = \int_{\Gamma} \boldsymbol{F}_{IB}(\boldsymbol{q},t)\, \delta(\boldsymbol{x} - \boldsymbol{X}(\boldsymbol{q},t))\, d\boldsymbol{q}, \tag{3}$$

where $\delta(\boldsymbol{x}) = \delta(x)\delta(y)$ is the Cartesian product of two one-dimensional Dirac delta functions.

Most papers in the immersed boundary literature assume that Γ has the same constant density ρ_f as the surrounding fluid, and hence Γ is neutrally buoyant. However, for the particle sedimentation application considered here, we must take Γ (or at least portions of it) to have density $\rho_s > \rho_f$ that is greater than that of the fluid. Consequently, the density of the fluid-solid composite material $\rho(\boldsymbol{x},t)$ is a variable quantity that may also be written in terms of a delta function convolution as [52]

$$\rho(\boldsymbol{x},t) = \rho_f + \Delta\rho(\boldsymbol{x},t)$$

where

$$\Delta\rho(\boldsymbol{x},t) = \int_\Gamma M(\boldsymbol{q})\,\delta(\boldsymbol{x}-\boldsymbol{X}(\boldsymbol{q},t))\,d\boldsymbol{q}.$$

The quantity $M(\boldsymbol{q}) \geqslant 0$ is the added Lagrangian mass density due to Γ, with $M = 0$ only for those components that are neutrally buoyant.

In all examples in this paper, we will take $M \equiv M_o$ (constant), and we also assume that the solid density is close to that of the fluid so that $\Delta\rho \ll \rho_f$. Consequently, it is reasonable to apply a Boussinesq approximation as in [25] so that the extra intertial term involving $\Delta\rho$ is neglected and the density on the left hand side of the momentum equations (1) is taken equal to the constant ρ_f:

$$\rho_f \frac{\partial \boldsymbol{u}}{\partial t} + \rho_f \boldsymbol{u}\cdot\nabla\boldsymbol{u} = \mu\nabla^2\boldsymbol{u} - \nabla p + \boldsymbol{f}_{IB} + \boldsymbol{f}_G. \tag{4}$$

The extra forcing term $\boldsymbol{f}_G$ derives from the force of gravity acting on the immersed boundary and can be written as [25]

$$\boldsymbol{f}_G(\boldsymbol{x},t) = -g\hat{k}\,\Delta\rho = -g\hat{k}\int_\Gamma M(\boldsymbol{q})\,\delta(\boldsymbol{x}-\boldsymbol{X}(\boldsymbol{q},t))\,d\boldsymbol{q}, \tag{5}$$

where $g = 980$ cm/s^2 is the gravitational acceleration and $\hat{k} = (0,1)$ is the unit vector in the vertical direction.

Finally, the immersed boundary is assumed to move with the fluid so that

$$\frac{\partial \boldsymbol{X}}{\partial t} = \int_\Omega \boldsymbol{u}(\boldsymbol{x},t)\,\delta(\boldsymbol{x}-\boldsymbol{X}(\boldsymbol{q},t))\,d\boldsymbol{x}, \tag{6}$$

which is simply the "no-slip" condition for fluid particles located adjacent to the immersed boundary.

In summary, the governing equations consist of (2), (4)–(6), with the IB force density being the only component that remains to be specified. Since it is easiest to write $\boldsymbol{f}_{IB}$ in discrete form, we will first derive the discretized governing equations, after which we will provide a specification for the IB force.

2.2. Numerical algorithm.

The algorithm we describe next is a semi-implicit scheme that is closely related to the method outlined in [41]. The fluid domain Ω is divided into an equally-spaced grid of points denoted by $\boldsymbol{x}_{i,j} = (x_i, y_j) = (ih_x, jh_y)$, with $h_x = L_x/N_x$, $h_y = L_y/N_y$, $i = 1,2,\ldots,N_x$, and $j = 1,2,\ldots,N_y$. We consider a time interval $[0,T]$ divided into equally-spaced points $t_n = n\Delta t$ with time step $\Delta t = T/N_t$ and $n = 0,1,2,\ldots,N_t$. We may then define discrete approximations of the velocity and pressure $\boldsymbol{u}^n_{i,j}$ and $p^n_{i,j}$ at points (x_i, y_j, t_n). The immersed boundary Γ is similarly discretized at points $\boldsymbol{X}_\ell$ for $\ell = 1,2,\ldots,N_b$, and the IB configuration and force density are approximated by $\boldsymbol{X}^n_\ell$ and $\boldsymbol{F}^n_\ell$ respectively.

Using the above notation, we introduce finite difference operators that approximate the spatial derivatives appearing in the governing equations. In particular, we define two one-sided difference approximations of the x–derivative of a grid quantity $w_{i,j}$

$$D^+_x w_{i,j} = \frac{w_{i+1,j} - w_{i,j}}{h_x} \quad \text{and} \quad D^-_x w_{i,j} = \frac{w_{i,j} - w_{i-1,j}}{h_x}, \tag{7}$$

as well as the centered approximation

$$D^0_x w_{i,j} = \frac{w_{i+1,j} - w_{i-1,j}}{2h_x}. \tag{8}$$

Analogous definitions apply for the y–derivative approximations D_y^+, D_y^- and D_y^0, and the gradient is replaced by the centered approximation $\nabla_h = (D_x^0, D_y^0)$. Finally, the delta function appearing in the integral terms is replaced by the regularized function

$$\delta_h(\boldsymbol{x}) = \frac{1}{h_x h_y}\phi\left(\frac{x}{h_x}\right)\phi\left(\frac{y}{h_y}\right), \tag{9}$$

where

$$\phi(r) = \begin{cases} \frac{1}{4}\left(1+\cos\left(\frac{\pi r}{2}\right)\right), & \text{if } |r| \leqslant 2, \\ 0, & \text{otherwise.} \end{cases} \tag{10}$$

We are now prepared to state the immersed boundary algorithm. In any given time step, we assume that values of the velocity $\boldsymbol{u}_{i,j}^{n-1}$ and IB configuration $\boldsymbol{X}_\ell^{n-1}$ are known from the previous step. These quantities are evolved to time t_n using the following procedure:

1. Compute the IB force density $\boldsymbol{F}_{IB,\ell}^{n-1}$ based on the configuration $\boldsymbol{X}_\ell^{n-1}$ as described in section 2.3.
2. Spread the IB force to the fluid grid points using a discretization of the integral in (3)

$$\boldsymbol{f}_{IB,i,j}^{n-1} = \sum_{\ell=1}^{N_b} \boldsymbol{F}_{IB,\ell}^{n-1}\,\delta_h(\boldsymbol{x}_{i,j} - \boldsymbol{X}_\ell^{n-1})\,A_b, \tag{11}$$

   and a similar approximation of the integral in (5) yields a formula for $\boldsymbol{f}_{G,i,j}^{n-1}$. The scaling factor A_b in both cases is inversely proportional to the number of IB points (N_b) and has a different interpretation depending on whether the immersed boundary is a 1D fiber (channel wall) or a 2D solid block (circular particle). In the case of a fiber A_b is a length, while for a solid region A_b is an area; in both cases, the factor A_b ensures that the formula (11) scales properly with the number of IB points and that it is a consistent approximation of the corresponding integral. More details on the precise form of (11) and the specification of A_b are provided in section 2.3.
3. Integrate the incompressible Navier-Stokes equations using a split-step projection scheme:
   (a) Compute an intermediate velocity $\boldsymbol{u}_{i,j}^{(1)}$ by applying the elastic and gravitational forces on the immersed boundary:

$$\rho_f\left(\frac{\boldsymbol{u}_{i,j}^{(1)} - \boldsymbol{u}_{i,j}^{n-1}}{\Delta t}\right) = \boldsymbol{f}_{IB,i,j}^{n-1} + \boldsymbol{f}_{G,i,j}^{n-1} \tag{12}$$

   (b) Apply an ADI discretization of the advection and diffusion terms:

$$\rho_f\left(\frac{\boldsymbol{u}_{i,j}^{(2)} - \boldsymbol{u}_{i,j}^{(1)}}{\Delta t} + u_{i,j}^{n-1} D_x^0 \boldsymbol{u}_{i,j}^{(2)}\right) = \mu D_x^+ D_x^- \boldsymbol{u}_{i,j}^{(2)}, \tag{13}$$

$$\rho_f\left(\frac{\boldsymbol{u}_{i,j}^{(3)} - \boldsymbol{u}_{i,j}^{(2)}}{\Delta t} + v_{i,j}^{n-1} D_y^0 \boldsymbol{u}_{i,j}^{(3)}\right) = \mu D_y^+ D_y^- \boldsymbol{u}_{i,j}^{(3)}. \tag{14}$$

   These equations represent a sequence of tridiagonal solves for $\boldsymbol{u}_{i,j}^{(2)}$ and $\boldsymbol{u}_{i,j}^{(3)}$.
   (c) Project the intermediate velocity $\boldsymbol{u}_{i,j}^{(3)}$ onto the space of divergence-free vector fields by:
      i. Solving the pressure Poisson equation

$$\nabla_h \cdot \nabla_h p_{i,j} = \frac{\rho_f}{\Delta t}\nabla_h \boldsymbol{u}_{i,j}^{(3)}. \tag{15}$$

      Note that $\nabla_h \cdot \nabla_h$ represents a wide finite difference stencil for the Laplacian involving the pressure values $p_{i,j}$, $p_{i-2,j}$, $p_{i+2,j}$, $p_{i,j-2}$ and $p_{i,j+2}$. Owing to the periodic boundary conditions on Ω, this equation is solved most easily and efficiently by means of the discrete Fourier transform, and making use of the FFT algorithm.

ii. Updating the velocity according to

$$\boldsymbol{u}_{i,j}^{n} = \boldsymbol{u}_{i,j}^{(3)} - \frac{\Delta t}{\rho_f} \nabla_h p_{i,j}. \tag{16}$$

4. Evolve the immersed boundary using

$$\boldsymbol{X}_{\ell}^{n} = \boldsymbol{X}_{\ell}^{n-1} + \Delta t \sum_{i,j} \boldsymbol{u}_{i,j}^{n}\, \delta_h(\boldsymbol{x}_{i,j} - \boldsymbol{X}_{\ell}^{n-1})\, h_x h_y. \tag{17}$$

This simple semi-implicit time discretization described above yields a solution that is first-order accurate in time. And although all spatial derivatives are approximated using second-order finite differences, the method is still only first-order accurate in space owing to errors in velocity interpolation near the immersed boundary that arise from the use of the regularized delta function. It is straightforward to increase the temporal accuracy to second order using an algorithm such as that proposed by Lai and Peskin [31], but it is much more difficult to increase the spatial accuracy [20]. Since the focus of the current study is to validate the general IB approach in the study of particle sedimentation, we have chosen to employ the simple scheme above, and leave for future work the implementation of higher order extensions to the algorithm.

2.3. Discrete IB force density for particle and channel walls.

We begin by describing the geometry for the particle sedimentation problem. Referring to Figure 2, we take a rectangular fluid domain of size $L_x \times L_y$ and place two vertical immersed fibers representing the channel walls a distance $W < L_x$ apart, symmetric relative to the channel centerline, and separated from the domain boundary by a narrow strip of fluid. With periodic boundary conditions applied on all sides of the domain, the channel walls naturally connect to each other across the top and bottom boundaries. A single, solid, circular particle of diameter D is initially located at the center of the channel. Later on, we will consider other initial configurations with one and two particles, but for now this will suffice to illustrate the calculation of the IB force density. This circular particle in 2D may be thought of as corresponding in 3D to a cross-section of a solid cylinder with infinite length.

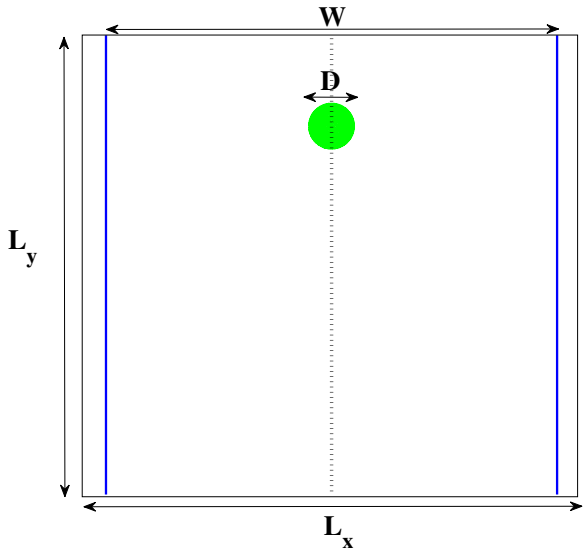

Figure 2: Initial geometry for the gravitational settling problem. The parallel channel walls are denoted by dashed vertical lines, separated by a distance W. The first test case has a single solid particle of diameter D that is released at time $t = 0$ along the channel centerline (which is indicated by a dotted line).

In our sedimentation model, the IB force density $\boldsymbol{F}_{IB}$ is the sum of two terms, $\boldsymbol{F}_{IB} = \boldsymbol{F}^{w} + \boldsymbol{F}^{c}$, where $\boldsymbol{F}^{w}$ represents the force density generated by the channel walls and $\boldsymbol{F}^{c}$ is that generated by the circular particle. These forces are discussed separately in the next two sections.

2.3.1. Elastic force from the channel walls, $\boldsymbol{F}^w$.

The vertical walls are discretized using an equally-spaced array of IB points that are initially at locations $\boldsymbol{X}_\ell^{w,L} = \left(\frac{1}{2}(L_x - W),\, \ell h_w\right)$ for the left wall, and $\boldsymbol{X}_\ell^{w,R} = \left(\frac{1}{2}(L_x + W),\, \ell h_w\right)$ for the right wall, where the wall point spacing is $h_w = L_y/N_w$ and $\ell = 1, 2, \ldots, N_w$. Each IB point is connected to a fixed "tether point" (at the same initial location) by a very stiff spring that exerts a force of the form

$$\boldsymbol{F}_\ell^{w,L} = \sigma_w(\boldsymbol{X}_\ell^{w,L} - \boldsymbol{X}_\ell), \tag{18}$$

where σ_w [g/cm s^2] is the spring stiffness and $\boldsymbol{X}_\ell$ is the moving IB point location. Any motion of the IB point away from corresponding the tether point location generates a spring force that drives it back towards the target, so that as long as σ_w is chosen large enough the wall points can be made to mimic a rigid structure. We emphasize that tether points neither move with the fluid nor generate any force themselves. A similar expression is developed for the force density at the right wall points, $\boldsymbol{F}_\ell^{w,R}$ so that the total wall force density may be written as

$$\boldsymbol{F}^w = \sum_{\ell=1}^{N_w} (\boldsymbol{F}_\ell^{w,L} + \boldsymbol{F}_\ell^{w,R}). \tag{19}$$

The natural choice of scaling factor in the force spreading step (11) is the wall point spacing, $A_b = h_w$.

2.3.2. Elastic force from the particle, $\boldsymbol{F}^c$.

The circular particle is represented by a collection of N_c Lagrangian points that lie on its circumference and throughout its interior. We make use of the unstructured triangular mesh generator DistMesh [34] that generates a nearly uniform triangulation such as that shown in Figure 3. The nodes of the triangulation are the IB points $\boldsymbol{X}_\ell$, for $\ell = 1, 2, \ldots, N_c$, while the edges of the triangles define a network of springs that maintains the shape of the particle. In addition to bearing IB spring forces, the network nodes are also employed in equation (5) to distribute added mass throughout the particle. In practice, we generate the

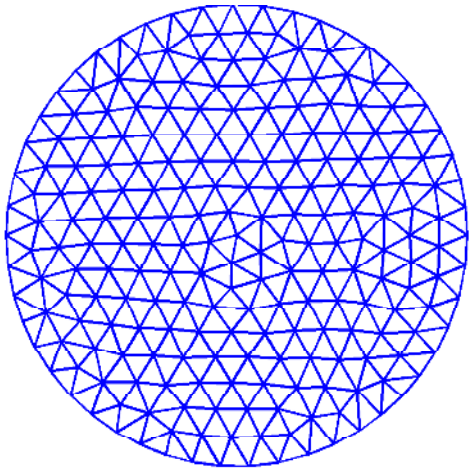

Figure 3: Uniform triangular mesh generated by `distmesh2d`.

triangulation by calling the Matlab function `distmesh2d` with the "scaled edge length function" `huniform` (a function provided by the authors that attempts to find a mesh that is as uniform as possible). We also

set the "initial edge length" parameter equal to $\frac{1}{3}\min(h_x, h_y)$, which ensures that the mesh obeys

$$\max_{k,\ell} |\boldsymbol{X}_k - \boldsymbol{X}_\ell| < \frac{1}{2}\min(h_x, h_y),$$

which is a standard "rule of thumb" that avoids leakage of fluid between IB points [35].

This form of particle discretization should be compared with the more common IB approach that uses an open circular ring of points with a freely-moving fluid inside, such as in [31, 49]. This approach has been criticised [22] for generating non-physical fluid motions inside the particle and in some cases leading to significant deviations in the shape of the particle. In contrast, our discretization of the particle interior with a network of IB springs suppresses this spurious fluid motion and also helps to maintain the rigidity of the particle boundary.

We now define the spring forces that act on the network, following the development of Alpkvist and Klapper for viscoelastic biofilm structures [2]. Let $\boldsymbol{d}_{\ell,m}(t) = \boldsymbol{X}_\ell(t) - \boldsymbol{X}_m(t)$ be the vector joining two IB points labeled ℓ and m, and let $d_{\ell,m}(t) = |\boldsymbol{d}_{\ell,m}(t)|$ be the corresponding distance. We assume that the spring network is initially in equilibrium (i.e., zero force) so that all springs have a resting length equal to their initial length, $d_{\ell,m}(0)$. Let $\mathbb{I}$ be an incidence matrix whose entries $\mathbb{I}_{\ell,m}$ are either 1 or 0 depending on whether or not points ℓ and m are connected, respectively. Then the force density acting on the ℓ^{th} IB point in the network is

$$\boldsymbol{F}^c_\ell = \sigma_c \sum_{\substack{m=1 \\ \mathbb{I}_{\ell,m}\neq 0}}^{N_b} \mathbb{I}_{\ell,m} \frac{\boldsymbol{d}_{\ell,m}}{d_{\ell,m}} (d_{\ell,m}(0) - d_{\ell,m}), \tag{20}$$

where the sum is taken only over those m for which $\boldsymbol{X}_m$ is connected to $\boldsymbol{X}_\ell$ in the network. We have also assumed that the spring stiffness σ_c [g/cm s^2] is constant for all network connections. The total elastic force density generated by all IB points making up the circular particle is then given by

$$\boldsymbol{F}^c = \sum_{\ell=1}^{N_c} \boldsymbol{F}^c_\ell. \tag{21}$$

The appropriate scaling factor for the force integral (11) is the average area of a triangular mesh cell, $A_b = \pi(D/2)^2/N_c$. A similar approach was employed by Hopkins and Fauci [25] to simulate a suspension of microbial cells that they treated as point particles.

3. Approximate formulas for settling velocity.

We next review some of the existing analytical and experimental results on the settling of a single particle falling under the action of gravity. The study of a spherical particle in an unbounded fluid medium in 3D is a classical problem that was considered by Stokes [43], who obtained a formula for the settling velocity that is now known as Stokes' law. We will first state Stokes' result and then modify it for a circular particle in 2D, which corresponds to an idealized "infinite cylinder" in 3D. We then consider the case of a circular particle falling in a bounded fluid domain between two vertical walls and then review several of the most commonly-used formulas for the "wall-correction factors" that have been obtained from either fitting to experimental data or using approximate analytical techniques. A fairly extensive overview of settling for cylindrical particles, including many of the wall correction formulas reported in the literature, is given by Champmartin and Ambari [10].

3.1. Stokes' law for a spherical particle in 3D.

There are two main forces acting upon a massive particle settling in a fluid: the gravitational force F_g, and the drag force F_d due to the "friction" between the particle and the fluid. A particle that is initially at rest will accelerate under the action of gravity, and as the particle begins to move through the fluid it

experiences a drag force in the direction opposite to its motion that increases with the speed of the particle relative to the fluid. If the drag force becomes large enough that it equals the gravitational force, then the two forces are in balance and no further acceleration occurs. The particle velocity in this equilibrium state is known as the settling or terminal velocity.

We take a sphere of diameter D and density ρ_s whose added mass relative to the fluid is $\frac{4}{3}\pi\left(\frac{D}{2}\right)^3(\rho_s-\rho_f)$. The net gravitational force acting on the sphere is

$$F_g = \frac{4\pi}{3}\left(\frac{D}{2}\right)^3 g(\rho_s - \rho_f), \tag{22}$$

and the corresponding drag force is

$$F_d = \frac{1}{2}C_d\rho_f V^2\pi\left(\frac{D}{2}\right)^2, \tag{23}$$

where C_d is the drag coefficient for a sphere and V is the velocity of the sphere relative to the fluid. The settling velocity V_s corresponds to the long-term steady state in which drag and gravity forces are in balance, so that $F_d = F_g$. By equating (22) and (23), we can solve for

$$V_s = \sqrt{\frac{4gD(\rho_s - \rho_f)}{3C_d\rho_f}}, \tag{24}$$

keeping in mind that the drag coefficient on the right hand side also typically depends on the settling velocity, V_s. Indeed, we know from [3] that the drag coefficient for a sphere can be approximated for small Reynolds number by

$$C_d = \frac{24}{Re} = \frac{24\mu}{\rho_f V_s D}, \tag{25}$$

where we have taken

$$Re = \frac{\rho_f D V_s}{\mu}, \tag{26}$$

based on the particle diameter. Substituting this expression into (24) and solving for V_s we obtain Stokes' law

$$V_s = \frac{gD^2(\rho_s - \rho_f)}{18\mu}, \tag{27}$$

which is valid for $Re \lesssim 0.1$.

3.2. Settling velocity for a circular particle in 2D.

A similar argument may be used to derive the corresponding expression for a circular particle in 2D. We begin by considering a cylinder with diameter D and length ℓ and take the limit as $\ell \to \infty$ in order to obtain a result that is relevant to our 2D geometry. The immersed cylinder has an added mass (relative to the fluid) of $m = \pi\left(\frac{D}{2}\right)^2\ell\,(\rho_s - \rho_f)$ for which the net gravitational force is

$$\widetilde{F}_g = \frac{\pi}{4}g\ell D^2(\rho_s - \rho_f), \tag{28}$$

and the drag force is

$$\widetilde{F}_d = \frac{1}{2}\widetilde{C}_d\rho_f\widetilde{V}^2 D\ell. \tag{29}$$

ρ_s	$\Delta\rho$	$\widetilde{V}_s$
1.01	0.01	0.0024
1.02	0.02	0.0045
1.03	0.03	0.0066
1.04	0.04	0.0086
1.05	0.05	0.0105

Table 1: Settling velocities $\widetilde{V}_s$ for a cylindrical particle, obtained by solving equation (32) with $\rho_f = 1$ and $D = 0.018$.

Notice that the cross-sectional area factor $\pi\,(D/2)^2$ for the sphere from (23) is replaced by $D\ell$ for the cylinder, and the tildes are used here to denote cylindrical quantities. We also make use of the drag coefficient for a cylinder from [3]

$$\widetilde{C}_d = \frac{8\pi}{Re\ln\left(\frac{7.4}{Re}\right)}, \tag{30}$$

which holds when $Re \ll 1$.

The settling velocity for the cylinder is then obtained by equating the gravitational and drag forces in (28) and (29), which yields

$$\widetilde{V}_s = \sqrt{\frac{\pi g D(\rho_s - \rho_f)}{2\widetilde{C}_d \rho_f}}. \tag{31}$$

Observe that the factor of length ℓ cancels in the above expression, so that this same expression is valid also for the 2D geometry in the $\ell \to \infty$ limit. Furthermore, this expression is the same as that for the sphere in (24) except that the factor $\sqrt{4/3}$ is replaced here with $\sqrt{\pi/2}$, and of course the cylinder drag coefficient is also different. When equations (30)–(31) are taken together, they reduce to a nonlinear equation in Re

$$f(Re) = Re - \frac{\rho_f g D^3(\rho_s - \rho_f)}{16\mu^2}\,\ln\left(\frac{7.4}{Re}\right) = 0, \tag{32}$$

which can alternatively be written as an equation in $\widetilde{V}_s$. It is easy to show that the function $f(x)$ is continuous on the interval $0 < x < \infty$ and has the following properties:

$$\lim_{x\to 0^+} f(x) = -\infty, \quad \lim_{x\to\infty} f(x) = +\infty \quad \text{and} \quad f'(x) > 0.$$

Therefore, f is guaranteed to have a unique positive real root by the intermediate value theorem.

Newton's method may be used to solve (32) for Re, and we find that any initial guess for Re suffices since the convergence is to rapid. Table 1 lists values of $\widetilde{V}_s$ from (32) for parameters $D = 0.018$ and ρ_s ranging from 1.01 to 1.05. As expected, the settling velocity increases with particle density as in the Stokes case.

3.3. Wall-corrected settling velocities.

In this section, we summarize a number of formulas that approximate settling velocity for a particle in a bounded fluid domain that consists of a channel with two parallel, vertical walls separated by a distance W. It is well-known that the bounding walls exert an additional retarding effect on a sedimenting particle [4, 11, 14, 23, 37, 45, 50] so that the settling velocity is lower in a channel than in an unbounded domain under the

same conditions. The effect of these wall interactions may be approximated by means of a "wall correction factor" λ, that is usually expressed in the form [4, 5]

$$\lambda(k, Re) = \frac{\widetilde{F}_d(k)}{\mu V_c}, \tag{33}$$

where $\widetilde{F}_d(k)$ represents a drag force per unit length, V_c is the terminal settling velocity in the channel, and $k = D/W$ is the dimensionless particle size with $0 < k < 1$.

Note that the factor $\lambda(k, Re)$ depends on both Reynolds number and particle size; however, it is well known [11] that at either very low or very high values of $\Re$, λ is nearly independent of the Reynolds number. In this study, we are concerned with the low Re regime and so it is reasonable to assume that λ depends on k only. Various formulas for the wall correction factor have been reported in the literature (see [4], for example) all of which have the same channel geometry as pictured in Figure 2. Some of the more common wall correction factors are listed below:

- White [50]: carried out experiments with various wires and ebonite rods in a channel containing viscous liquids such as glycerin and paraffin. He obtained the following experimental fit for the drag force on a cylinder

  $$\lambda(k) = \frac{-6.4}{\ln(k)}, \tag{34}$$

  whose domain of validity is restricted to $0 < k < 0.2$.

- Faxén [14, 23]: derived an approximate analytical solution of the Stokes equations, from which he obtained

  $$\lambda(k) = \frac{-4\pi}{0.9157 + \ln(k) - 1.724k^2 + 1.730k^4 - 2.406k^6 + 4.591k^8}. \tag{35}$$

  Some authors claim that this approximation is valid for k as large as 0.5 [4, 53]. However, others cite an upper bound of $k = 0.3$ or even lower [37] which is more in line with our numerical simulations (see Figure 8 in Section 4).

- Takaisi [45]: used an analytical solution of Oseen's equations to obtain the approximation

  $$\lambda(k) = \frac{-4\pi}{0.9156 + \ln(k)}, \tag{36}$$

  which is restricted to $0 < k < 0.2$. He also performed a comparison with White's experimental fit and showed that the two expressions match reasonably well when $k < 0.05$.

If we now consider $\lambda(k)$ to be a known function of the dimensionless particle size k, then equation (33) can be solved for the drag force per unit length as

$$\widetilde{F}_d(k) = V_c \mu \lambda(k).$$

Equating this expression with the gravitational force

$$\widetilde{F}_g = \frac{\pi}{4} g D^2 (\rho_s - \rho_f),$$

we find the following formula for the confined (or wall-corrected) terminal settling velocity of a cylinder

$$V_c = \frac{\pi g D^2 (\rho_s - \rho_f)}{4\mu\lambda(k)}. \tag{37}$$

In the next section, this expression will be compared with numerically simulated values for the three choices of $\lambda(k)$ listed above.

4. Numerical results: Single particle case.

In this section, we concentrate on a single particle that settles under the influence of gravity. Two initial configurations are investigated: one a symmetric case in which the particle is released along the centerline, and a second asymmetric case where the particle is released from an off-center location.

We restrict ourselves to a low Reynolds number regime corresponding to $Re \lesssim 7$, where Re refers to a "final" Reynolds number that is based on the vertical velocity after a particle has achieved its terminal settling velocity. Unless otherwise indicated, we choose physical parameters $\rho_f = 1$, $\rho_s = 1.01$ and $D = 0.08$. The wall and particle IB spring stiffness values are taken large enough that the walls and particle boundary do not deform "too much" from their initial shapes – taking $\sigma_w = \sigma_c = 3 \times 10^4$ keeps the relative error in these boundary shapes to within approximately 0.2%.

Except for the convergence study in the next section, most of our simulations are performed at the same grid resolution of $h_x = h_y = 0.0083$ and with a time step of $\Delta t = 10^{-5}$. We also select the number of IB points for the two channel walls (N_w) such that the ratio of spacing between wall points to fluid grid size is $h_w / \min(h_x, h_y) \approx \frac{1}{3}$ – this ratio is well within the factor of $\frac{1}{2}$ that is recommended to avoid leakage of fluid between IB points [35]. We also adjust the number of IB points for the particle (N_c) until the initial mesh computed by DistMesh satisfies the same criterion.

4.1. Convergence study

We begin by performing a convergence study that validates the spatial accuracy of our numerical method. As mentioned earlier in section 2.2, the IB algorithm being employed here is well-known to be first order accurate in space. To verify this result, we select a sequence of fluid grids with $N_x = N_y = 56$, 112, 224 and 448 on a square domain with side length $L_x = L_y = 1$, and use the settling velocity V_s as a representative measure of the solution for each case. The difference between values of V_s on successive grids is calculated and the results are plotted in Figure 4, which demonstrates that our numerical solution converges as the grid spacing is reduced. The curve is nearly a straight line on a log-log scale, and the slope of 0.79 obtained from a least squares fit suggests that our implementation of the IB method is close to the expected first-order accuracy. Similar convergence rates are observed for other quantities such as fluid velocity, IB position, etc.

4.2. Comparison with Stokes' law.

We aim next to validate the numerical method against the settling velocity $\widetilde{V}_s$ for a cylinder in an unbounded medium. However, we recall that our doubly periodic geometry implies that a single particle actually corresponds to an infinite array of sedimenting particles. Therefore, in the absence of solid boundaries or any other mechanism for dissipating energy, the net effect of gravity acting on such an infinite array of mass-bearing particles will be to accelerate the particles and the surrounding fluid indefinitely. This situation is clearly non-physical, and so instead we introduce walls into the domain that are situated "far enough" from the particle so as to minimize wall-particle interactions and yet still permit the particle to reach its natural terminal velocity. To this end, we take a square domain with side length $L_x = L_y = L$ that contains two vertical walls separated by a distance $W = L - 0.04$, and perform a sequence of computations with successively larger L. In particular, we fix the particle diameter at $D = 0.018$ cm and vary L between 1 and 7 cm. The fluid viscosity here and in the next section is $\mu = 1$ g/cm s, which we remark is much larger than in later sections because a meaningful comparison to $\widetilde{V}_s$ is only possible at low Reynolds number.

The computed values of settling velocity are summarized in Table 2, from which we observe that as L increases V approaches a limiting value of roughly 0.001674 cm/s. The results have clearly converged on the largest domain size, but the limiting value of V is significantly less than the Stokes settling velocity from equation (31), $\widetilde{V}_s = 0.00239$ cm/s. We suspect that the discrepancy is due to a combination of effects arising from grid resolution, including the first-order dispersive errors in our numerical scheme and the increase in the effective thickness of the walls and particle owing to the delta function smoothing width (this last effect is discussed further in section 4.3.2).

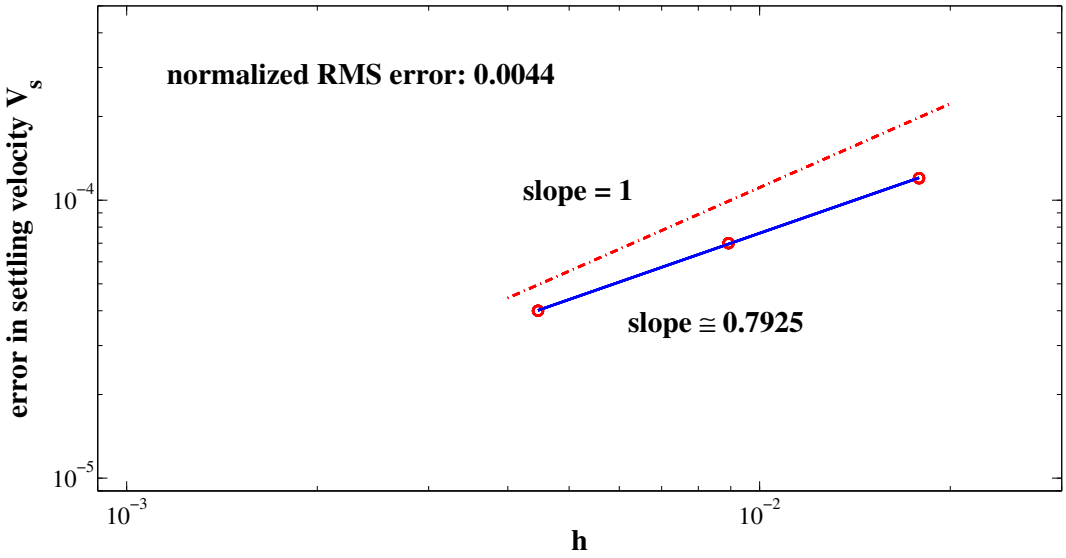

Figure 4: A convergence study in the settling velocity V_s on a sequence of grids. The difference in values of V_s on two successively finer grids is plotted versus the grid spacing h. A straight line with slope 1 corresponding to a first-order method is shown for comparison purposes.

L	computed V
1	0.001230
2	0.001462
3	0.001565
4	0.001635
5	0.001673
6	0.001674
7	0.001674

Table 2: Computed settling velocity as a function of domain size L for $D = 0.018$.

4.3. Single particle initially along the centerline.

We next consider the channel domain pictured in Figure 2 wherein the particle is initially released along the center of the channel. In this case, the symmetry suggests that any forces generated by particle-wall interactions are balanced and so the particle should fall along the centerline without veering to either side. We perform a number of sensitivity studies that investigate the effect of parameters such as the fluid domain size $[0, L_x] \times [0, L_y]$, density difference $\Delta\rho$, and relative particle size k on the settling velocity. As in the previous section, simulations are restricted to low Reynolds number by taking $\mu = 1$.

4.3.1. Dependence of settling velocity on density difference $\Delta\rho$.

For a fixed channel size with $W = 0.98$ and $L_x = 1$, we vary $\Delta\rho$ between 0.01 and 0.17. The plot of settling velocity in Figure 5 shows that the wall-corrected settling velocity V_c increases linearly with $\Delta\rho$, which is consistent with equation (37). We also consider the effect of changes in the channel length by taking $L_y \in \{3, 10, 16\}$, which indicates that the influence of periodic copies in the y–direction is most greatest for the shortest channel ($L_y = 3$) which also exhibits the highest settling velocity. As the channel length is increased, the settling velocity decreases until by $L_y = 16$ the results appear to have converged and are incidentally closest to the result predicted by Faxén's formula (35).

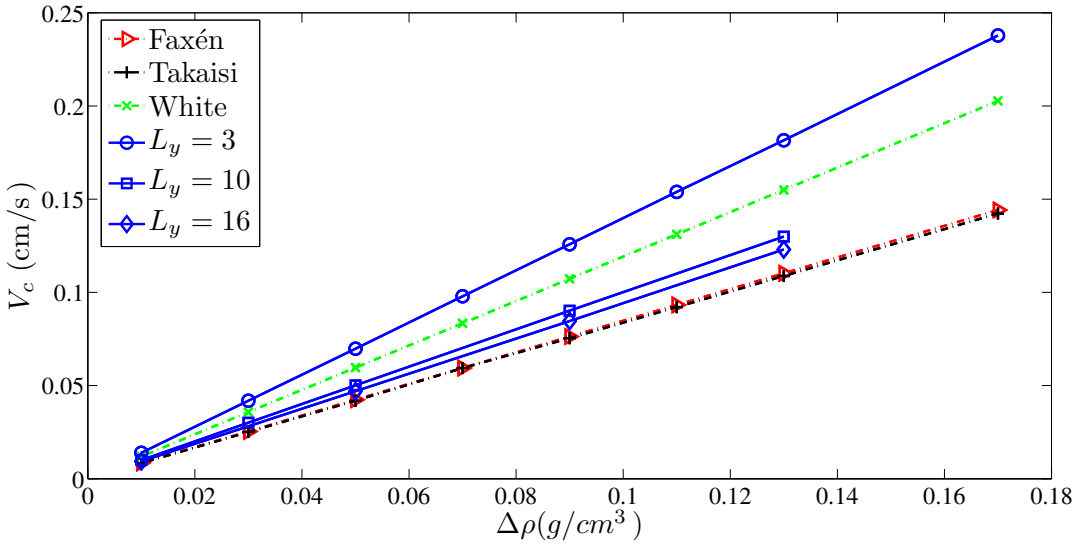

Figure 5: Settling velocity in a channel as a function of $\Delta\rho$. parameter values: $L_x = 1$, $L_y \in \{3, 10, 16\}$, $D = 0.1$, $W = 0.98$, $k = 0.102$.

4.3.2. Dependence of settling velocity on particle size k.

As mentioned earlier in section 3.3, the work of Faxén, White, Takaisi, and others suggests that λ depends only on k at low values of Reynolds number. This motivates our next sensitivity study of the effect of dimensionless particle size, for which we again fix the channel width at $W = L_x - 0.04$, and then vary k by choosing values of particle diameter $D \in [0.018, 0.96]$. Alongside our computational results in Figure 6, we have displayed corresponding estimates of the confined settling velocity V_c calculated using equation (37) with the three wall correction factors (34)–(36). The unbounded cylindrical settling velocity $\widetilde{V}_s$ is also included for comparison purposes, which clearly diverges from the wall-corrected values away from $k = 0$. For these simulations, Re was in the range $[1.2 \times 10^{-5}, 1.8 \times 10^{-2}]$.

Our computed results match most closely with Faxén's formula, which is most often cited as the most accurate approximation for the wall-corrected settling velocity. We also performed a study of the effect of changes in the channel length L_y, in order to determine the effect of any possible interference between vertical

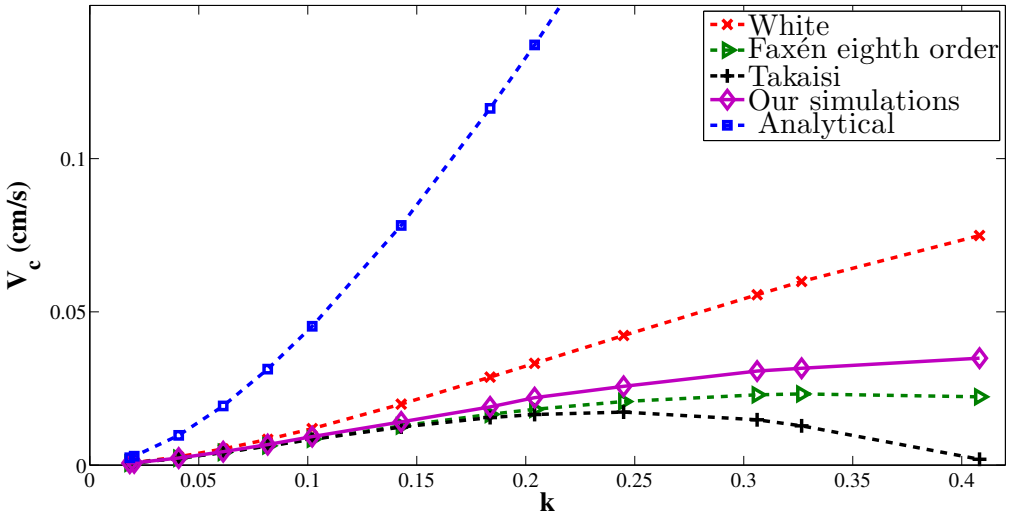

Figure 6: Variation of settling velocity with k for the computed results and various analytical expressions. Parameter values: $L_x = 1$, $L_y = 16$, $\mu = 1$.

periodic copies of the particle due to the periodicity assumption. Results for $L_y \in [1, 16]$ are displayed in Figure 7 which clearly show that our computed settling velocity converges to a value quite close to that predicted by Faxén's formula when $k \lesssim 0.2$.

On the other hand, there remain significant deviations between Faxén's results and our computations for values of k larger than 0.2, as demonstrated in Figure 8. Faxén's settling velocity levels out and attains a maximum near $k = 0.3$ and then falls to zero near $k = 0.6$. In contrast, our computed settling velocity reaches a maximum that is roughly 60% larger ($V_c \approx 0.035$) and plateaus for k roughly in the range $[0.4, 0.8]$.

Our computed settling velocity only drops to zero when k is very close to 1, which is easily justified since the particle must come to a stop as it come into direct contact with the stationary walls. However, our results in Figure 8 show that V_c actually tends to zero not at $k = 1$ but rather $k \approx 0.96$. The reason for this apparent reduction of 0.04 in the channel width is that the approximate delta function in our numerical scheme has a finite smoothing width that has the effect of introducing an extra "effective thickness" to both the walls and the particle. The numerical simulations in [42] show that when using the cosine delta function, the effective thickness of an immersed boundary is approximately $1.6h$, where h is the fluid grid spacing[1]. Consequently, a particle with diameter D should have an effective diameter of roughly $D_{\mathit{eff}} \approx D + 3.2h$, while the walls should each extend an additional distance of $3.2h$ into the channel. Taken together this suggests a total reduction of $6.4h$ in the effective channel width, which for $h = 0.0083$ equals approximately 0.053. This is not far away from the observed reduction of 0.04.

We summarize the behavior from our numerical simulations as follows:

- For small particle diameters corresponding to $k \in [0, 0.2]$, the particle is far enough from the channel walls that the retarding effects of wall drag are not as prominent. In this range, the dependence of the settling velocity is roughly proportional to k, which is consistent with Faxén's result.

- For intermediate values of k, roughly in the range $[0.4, 0.8]$, the settling velocity has attained a maximum value and remains approximately constant. For these particle sizes, the interactions with the walls are at long range and are mediated by the fluid.

[1]Note that the effective thickness depends on the choice of regularized delta function. Bringley [8] computed an effective thickness closer to $1.25h$ for a different but closely-related approximate delta function.

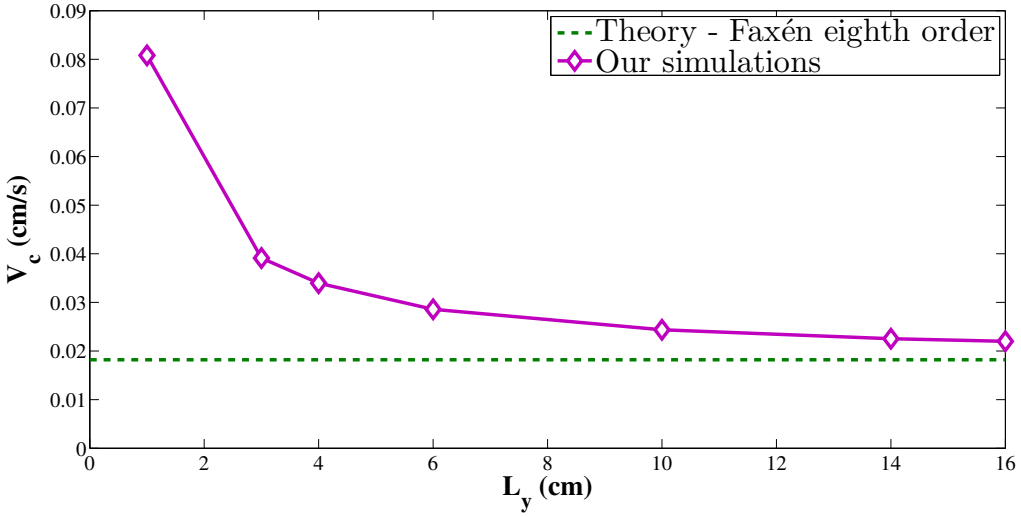

Figure 7: Effect of increasing the channel length L_y and hence reducing the impact of the periodic copies in y. Parameter values: $\mu = 1$, $L_x = 1$, $D = 0.2$, $W = 0.98$, $k = 0.2041$.

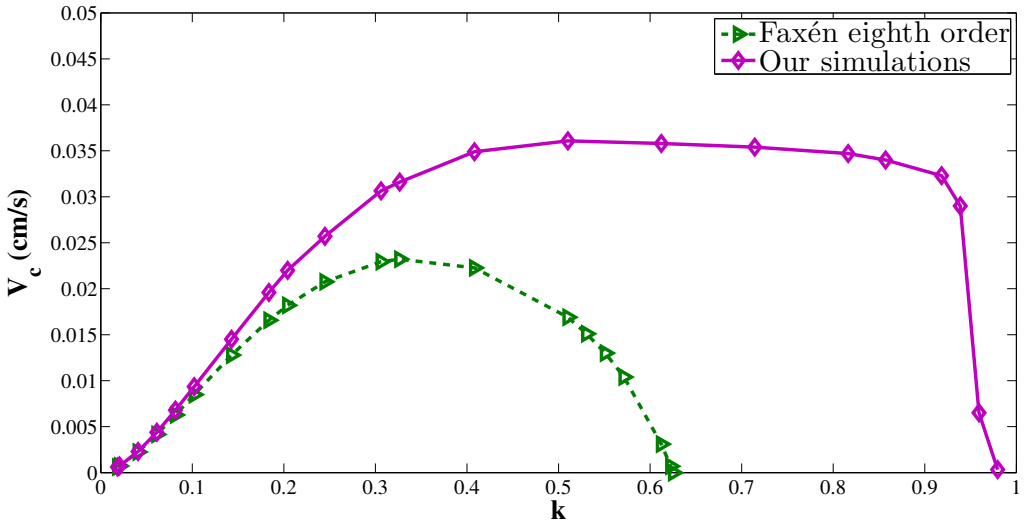

Figure 8: Plot of settling velocity versus k, comparing our simulations to Faxén's approximation. Parameter values: $L_x = 1$, $L_y = 16$, $\mu = 0.01$.

- For values of $k \in [0.8, 1.0]$, the particle is very close to the walls, giving rise to close-range interactions that slow the particle significantly.

Of course, the validity of Faxén's approximation is limited to $k \lesssim 0.2$ and so it is no surprise that our results differ so much for larger k.

4.4. Single particle initially off-center.

In this section, we consider an asymmetry initial condition in which the particle is released from an off-center location. In Figure 9, the initial configuration labeled "$t = 0$ s" shows the particle a distance $W/2$ to the left of center. The diameter of the particle is taken to be $D = 0.08$ cm, the channel length is $L_y = 3$, and we consider two different channel widths, $W = 4D$ and $8D$. We also vary Reynolds number by taking values of the viscosity $\mu \in [0.006, 0.018]$ g/cm s. This choice of parameters allows us to draw a comparison with the analytical and experimental results reported by Sucker and Brauer [44], as well as numerical simulations of Feng et al. [16].

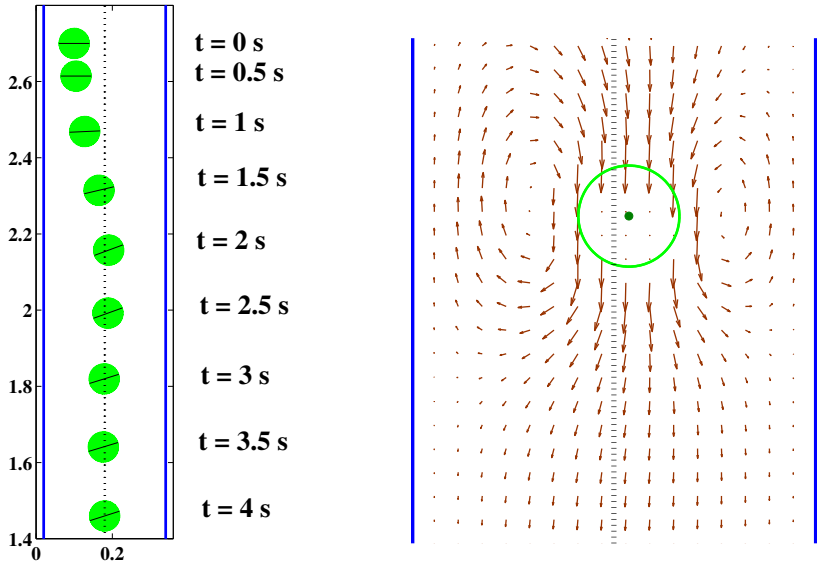

Figure 9: (Left) Settling dynamics for a single particle released off-center, in a channel of width $W = 4D$ and $Re = 4.9$. The solid line drawn through the center of the particle highlights the rotational motion. (Right) Velocity vector plot at time $t \approx 2$ s.

The settling dynamics are pictured in Figure 9 for $W = 4D$ and $Re = 4.9$. As the particle falls, it initially drifts to the right toward the channel centerline, eventually attaining its terminal settling velocity there. The plot of particle trajectories in Figure 10 shows that the particle actually undergoes a damped oscillation about the channel centerline with an initial overshoot. Simulations were also performed for three other Reynolds numbers, $Re = 2.2$, 3.7 and 4.4, and the corresponding trajectories in Figure 10 show that increasing Re leads to larger oscillations about the centerline. For the smallest value of $Re = 2.2$, the particle trajectory undergoes a nearly monotonic approach toward the centerline; in an analogy with simple harmonic oscillation, this behavior can be described as an overdamped oscillation.

In addition to the vertical and horizontal translations of the center of mass, the particle also undergoes a small-amplitude rotational motion as it settles, which can be seen by tracking the progress of the straight line drawn through the center of the particle in Figure 9. This rotation can be more easily seen in the plot of angular velocity in Figure 11 for the $Re = 4.9$ case. Initially, as the particle drifts from its starting location toward the centerline, it experiences a slight counter-clockwise rotation. As the particle approaches

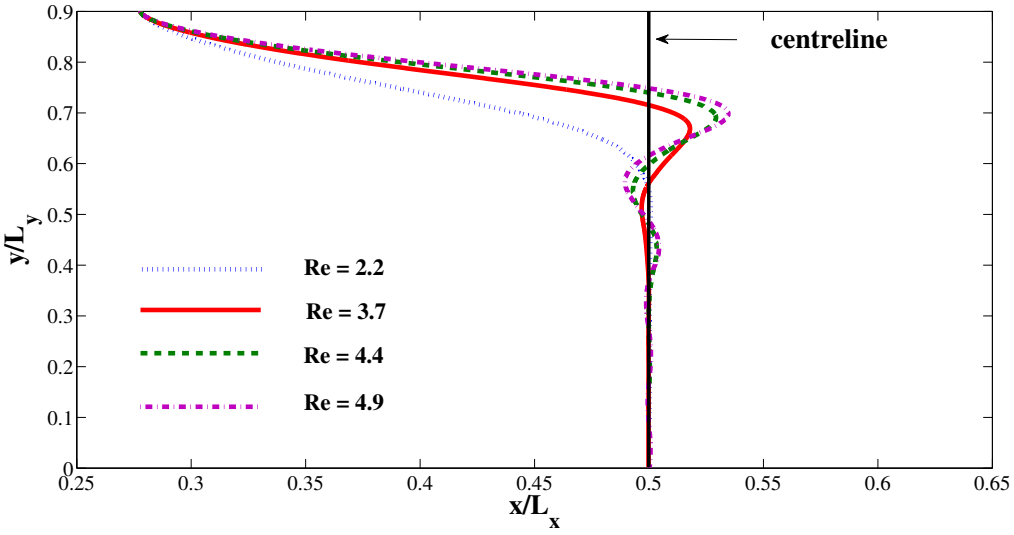

Figure 10: Settling trajectories for an off-center particle at different Reynolds number, in a channel of width $W = 4D$.

its equilibrium horizontal location, the rotation slows and the particle ends up with an orientation that is slightly tilted relative to the initial state.

We next perform simulations on a channel twice as wide ($W = 8D$) and take four different values of Reynolds number, $Re = 1.5$, 2.4, 4.2, and 6.4. The particle trajectories are shown in Figure 12 where we observe that in contrast with the $W = 4D$ results in Figure 10, there is no overshoot of the centerline even for the highest value of Re. We attribute this behavior to the fact that in a wider channel, the hydrodynamic interactions between wall and particle that drive the horizontal motions are substantially weaker. The plot of angular velocity in Figure 13 exhibits slightly different dynamics than the narrower channel, although the amplitude of the rotational motion is at least an order of magnitude smaller. This is to be expected since the rotational motion is also driven by the wall-particle interactions which are weaker for the wider channel case.

We conclude our examination of the single-particle settling dynamics by comparing in Figure 14 the drag coefficients for the two different channel widths considered above, based on the formula $\widetilde{C}_d = \pi(\rho_s - \rho_f)gD/(2\rho_f V_c^2)$ derived from equation (31). We have also included in this figure values of the drag coefficient taken from the following two papers:

- Feng, Hu and Joseph [16], who performed numerical simulations using a finite element method for a single particle settling in channels of width $4D$ and $8D$. Because we will refer to this paper so often, we will refer to it with the abbreviation FHJ.

- Sucker and Brauer [44], who developed an empirical formula that is a fit to experimental data for the cylinder in a very large fluid domain. They also developed an approximate analytical formula for an unbounded domain that matched closely with the experimental data.

Our simulations match reasonably well with those of FHJ particularly for the $W = 8D$ channel in the large L_y limit. Sucker and Brauer's empirical formula clearly deviates from both results because it applies strictly only to unbounded domains. While these results are encouraging, a much more comprehensive comparison is needed in order to draw any solid conclusions about the accuracy of our numerical approach.

(a)

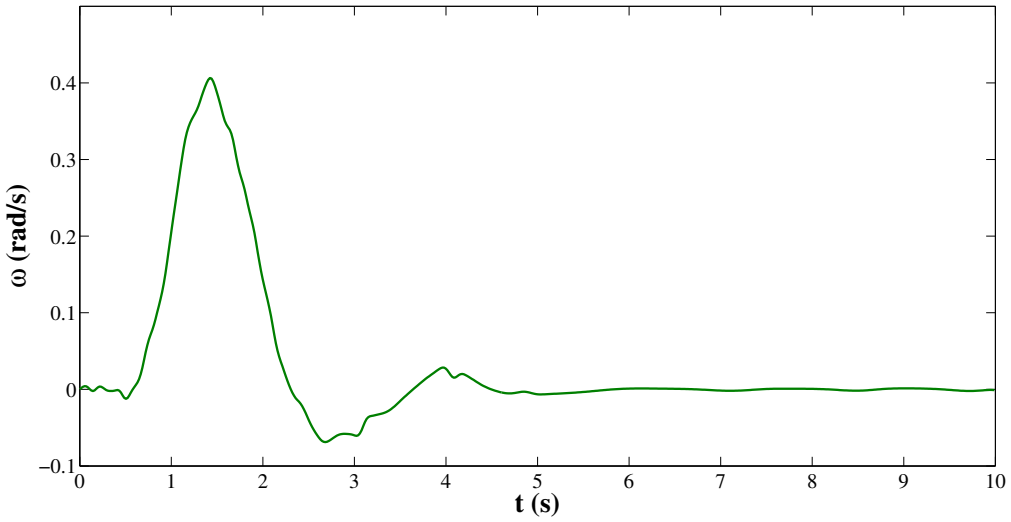

(b)

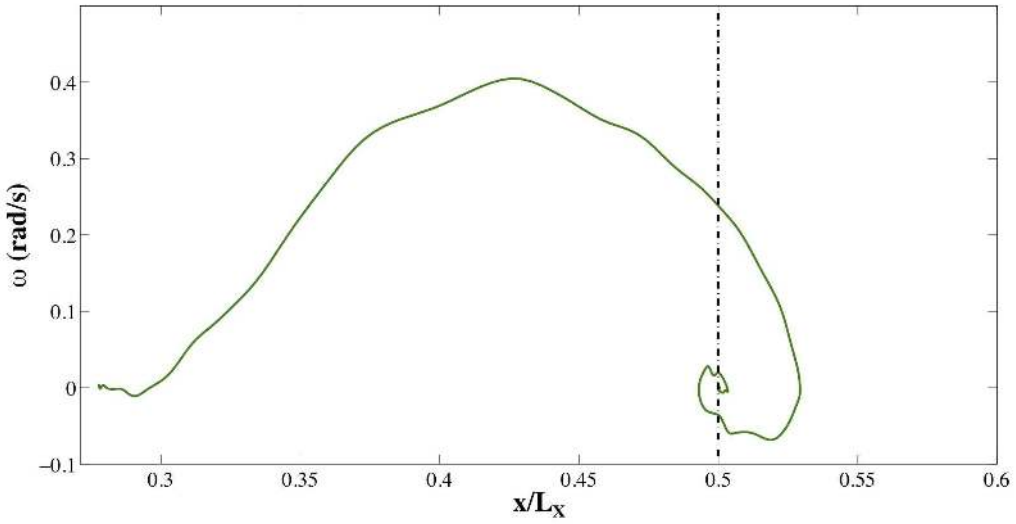

Figure 11: Plots of the angular velocity ω in rad/s, for a single particle released from an off-center location, with $W = 4D$ and $Re = 4.9$. Positive ω corresponds to counter-clockwise rotation. (a) Variation of angular velocity with time. (b) Angular velocity versus horizontal location, where the dashed line represents the channel centerline.

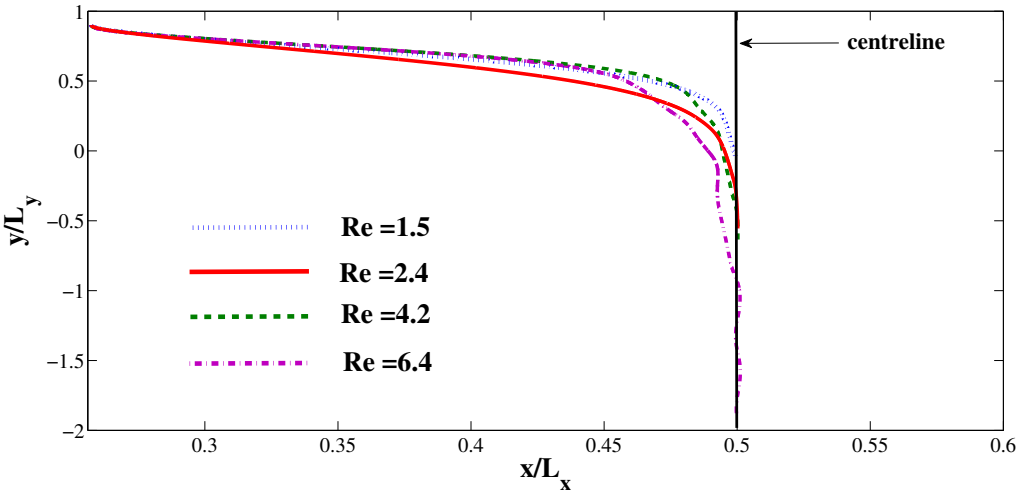

Figure 12: Settling trajectories for an off-center particle at different Reynolds number and in a channel of width $W = 8D$.

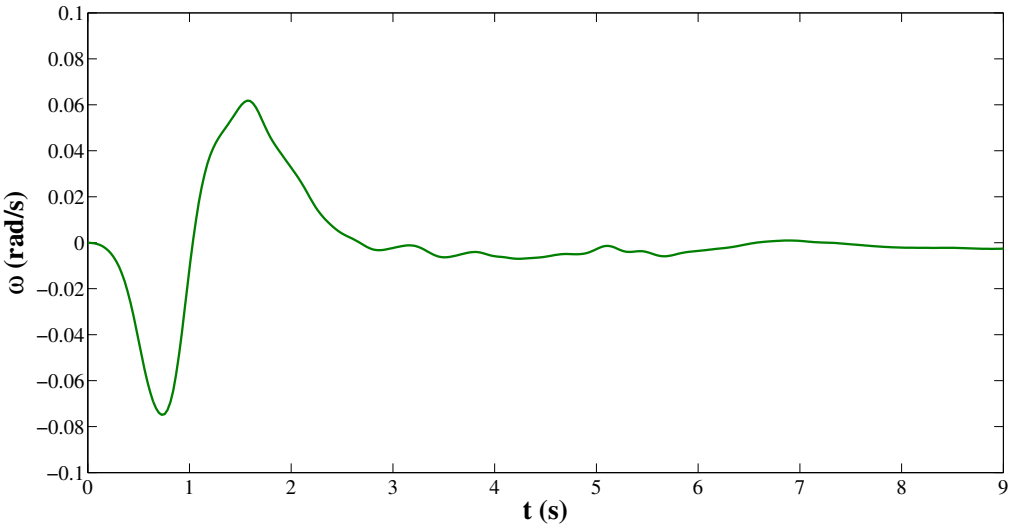

Figure 13: Plot of angular velocity ω for a single particle released from an off-center location, with $W = 8D$ and $Re = 6.4$.

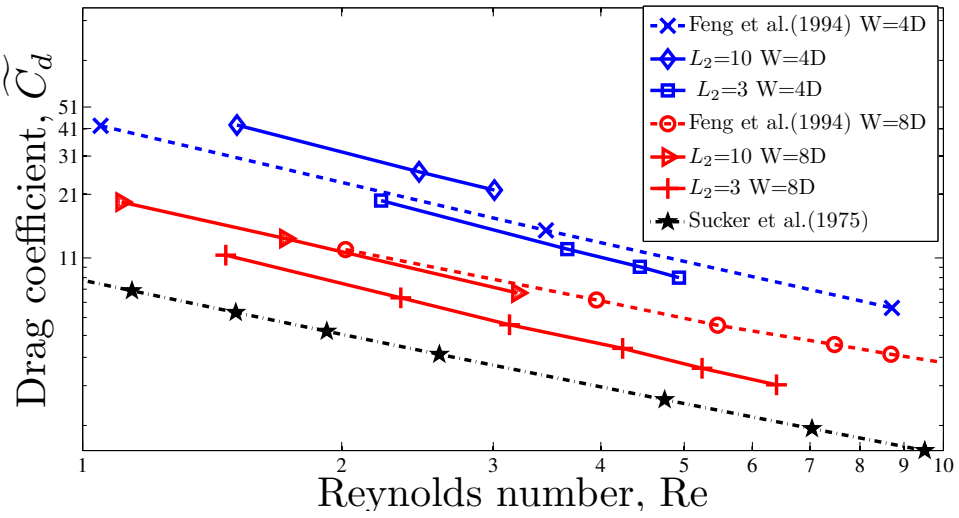

Figure 14: Comparison of drag coefficients for a single particle settling in channels of width $4D$ and $8D$, on a log–log scale. The experimental correlation of Sucker and Brauer [44] and numerical results from FHJ [16] are included for comparison purposes (reproduced with permission). Parameter values for our simulations: $D = 0.08$, $L_y = 3$, $L_x = 0.36$ (when $W = 4D$) and $L_x = 0.68$ (when $W = 8D$).

5. Numerical results: Two particle case.

This section investigates the interactions between two circular particles with identical diameter D that are settling in a channel of length $L_y = 3$. We consider several initial configurations pictured in Figure 15, and again compare the solution at different values of Reynolds number by varying viscosity over the range $\mu \in [0.0015, 0.16]$.

We begin by describing a well-known phenomenon in particle suspension flows wherein pairs of particles interact and undergo a "drafting, kissing and tumbling" behavior (which we abbreviate by DKT). This phenomenon has been established experimentally in papers such as [17, 29] and demonstrated numerically in [16], and can be justified physically as follows. The leading particle creates in its wake a reduction of pressure as it falls under the influence of gravity. Provided that the trailing particle is close enough to interact with this wake, it experiences a smaller drag force than the leading particle. As a result the trailing particle falls faster and the particles approach each other – this is the initiation of the "drafting phase". As the distance between the particles decreases, they eventually become close enough to nearly touch, which is referred to as "kissing". The kissing particles momentarily form a single longer body that is aligned parallel with the flow; however, this parallel arrangement is unstable and the particles eventually tumble relative to each other and swap leading/trailing positions – this is the "tumbling phase". The particles subsequently separate and one of two things happens: either the DKT process repeats, or the particles continue to separate until the interaction force becomes so weak that they fall independently at their "natural" wall-corrected vertical settling velocity [38].

The simulations in this section are performed using the four initial configurations depicted in Figure 15:

(a) Aligned vertically, one above the other along the channel centerline.
(b) Aligned vertically, but shifted to the left to a position midway between the channel centerline and the left wall.
(c) Aligned horizontally, and placed symmetrically about the centerline.
(d) Aligned horizontally, but shifted to the left of center.

In all cases, the particle diameter is $D = 0.08$ cm and the initial separation distance between the centers of mass of the two particles is $2D$. As in the previous section, we also consider two channel widths, $W = 4D$ and $W = 8D$.

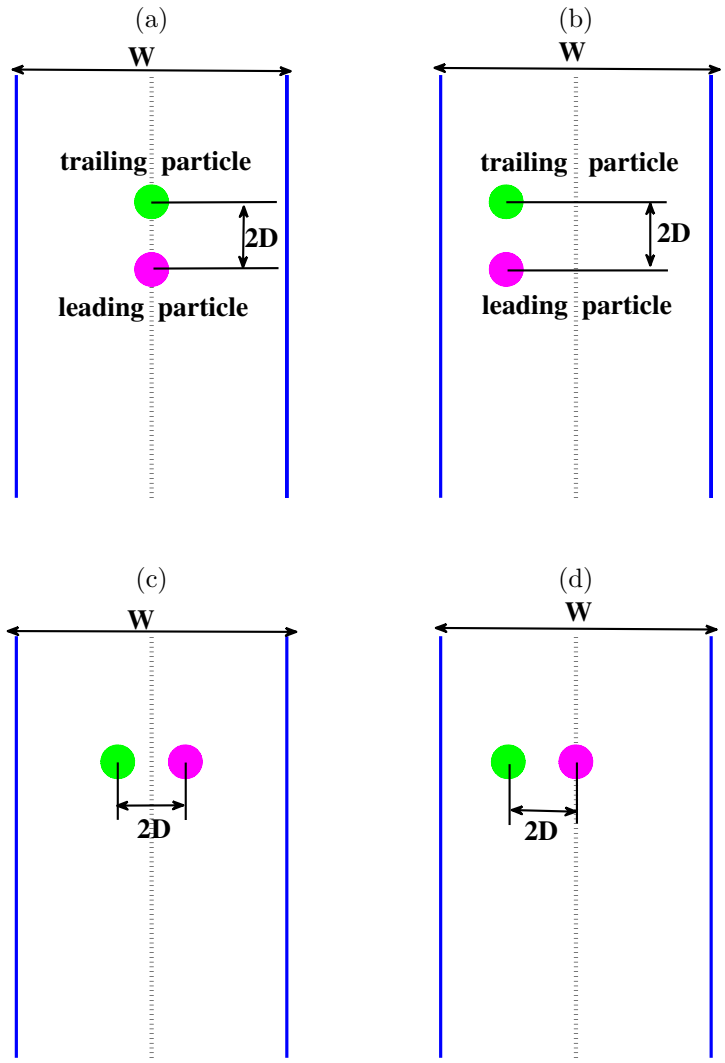

Figure 15: Four initial configurations for the two-particle settling problem, where the particle centers are separated by a distance $2D$: (a) aligned vertically, along the channel centerline; (b) aligned vertically, offset to the left of center; (c) aligned horizontally, symmetric about the centerline; (d) aligned horizontally, offset to the left of center.

5.1. Two vertically-aligned particles, released along the centerline.

As a first test of the two-particle case, we use the initial set-up shown in Figure 15(a) wherein the particles are both released along the centerline with their centers of mass separated vertically by a distance $2D$. We perform simulations with channel width $W = 8D$ and three different Reynolds numbers, $Re = 3$, 14 and 80.

Starting with the smallest value of $Re = 3$, we find that both particles remain along the channel centerline throughout the simulation, and while drafting and kissing behavior is observed, no tumbling occurs. As seen in Figure 16(a), the trailing particle approaches quite close to the leading particle, but never touches it. This is because of the increase in the effective diameter of the particle owing to the delta function smoothing radius, as was discussed already at the end of section 4.3.2. After kissing, the particles continue to fall as a single body with no significant relative motion, except for a very slight "wobble" that corresponds to a small-amplitude oscillation in the orientation angle (refer to the angular velocity plot in Figure 16(b)). This motion can be attributed primarily to oscillations of the IB points making up the particles that arises from the IB spring forces driving slight deviations from the equilibrium (stress-free) state; this is an artifact of the IB method that is not present in actual solid particles.

Upon increasing the Reynolds number to $Re = 14$ the dynamics become much more complex. The trailing particle catches up with and subsequently passes the leading particle at time $t \approx 11$ s, breaking the left-right symmetry. This tumbling behavior is evident in Figure 17(a) where the vertical separation distance becomes negative. After the first tumble, the particles separate horizontally and move to locations symmetrically opposite each other relative to the centerline and separated by a horizontal distance of roughly 0.27 cm. They continue to fall vertically at approximately the same x locations, and for the next 20 seconds they exchange leading and trailing positions via a small periodic variation in the vertical velocity whose amplitude decreases in time. By time $t \approx 35$ s, the particles have essentially reached a steady state in which they are falling at constant velocity and maintaining a constant separation distance (refer to Figure 17(b)).

The angular velocity plot in Figure 17(c) shows that both particles experience a significant rotation during the tumbling phase that is several orders of magnitude larger than the small "wobbling" motion observed in the $Re = 3$ case. In fact, the growth of this rotational motion appears to be connected with the breaking of the horizontal symmetry that initiates the tumbling motion. By time $t = 15$ s, the rotational motion has subsided.

Because of the symmetry in both the initial conditions and the governing equations, one would expect that the numerical solution should remain symmetric for all time, regardless of Reynolds number. The most likely source of asymmetry that initiates the tumbling behavior observed in the higher Re simulation is numerical error – these errors are sufficiently damped out when $Re = 3$, but remain large enough to initiate tumbling at $Re = 14$. This conjecture is borne out by the simulations in section 5.2, where two particles are aligned vertically and released off-center. We have nonetheless shown the results for this symmetric initial condition since it is commonly studied in other simulations [16].

As the Reynolds number is increased yet further to $Re = 80$, we observe in Figure 18 another qualitative change in solution behavior that is most easily seen in the sequence of snapshots collected in Figure 19. The two particles begin with a DKT exchange such as that observed for $Re = 14$, however this occurs as the two particles drift together toward the left channel wall (instead of toward the channel centerline). Following that, the particles drift reverse direction toward the right wall and undergo a second DKT exchange, after which the particle that was initially trailing ends up in the lead. These two DKT exchanges are accompanied by a back-and-forth rotational motion of each particle that has an amplitude similar in size to the $Re = 14$ case (refer to Figure 18(b)). Once again, it appears to be growth in the small "wobble" in the particle angular velocity plot that initiates tumbling. We also observe that when a particle nears the left wall it experiences a clockwise rotation, while the direction of rotation is reversed near the right wall – this is consistent with physical intuition, which suggests that wall drag arising from the no-slip condition at the channel wall should cause a rolling-type motion as the portion of the particle closest to the wall slows down.

FHJ [16] have performed a similar computation at $Re = 70$ (for the same symmetric initial conditions) that exhibits results consistent with ours up to time $t \approx 5.4$ s. However, they terminate their computation at this point and there is no indication in their paper of the subsequent dynamics. We have computed beyond

(a) Vertical separation distance

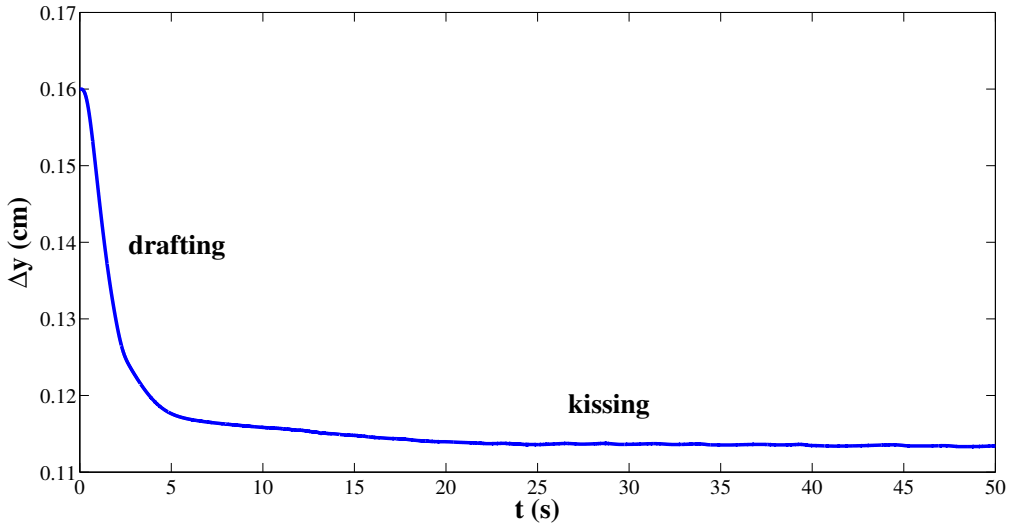

(b) Angular velocities

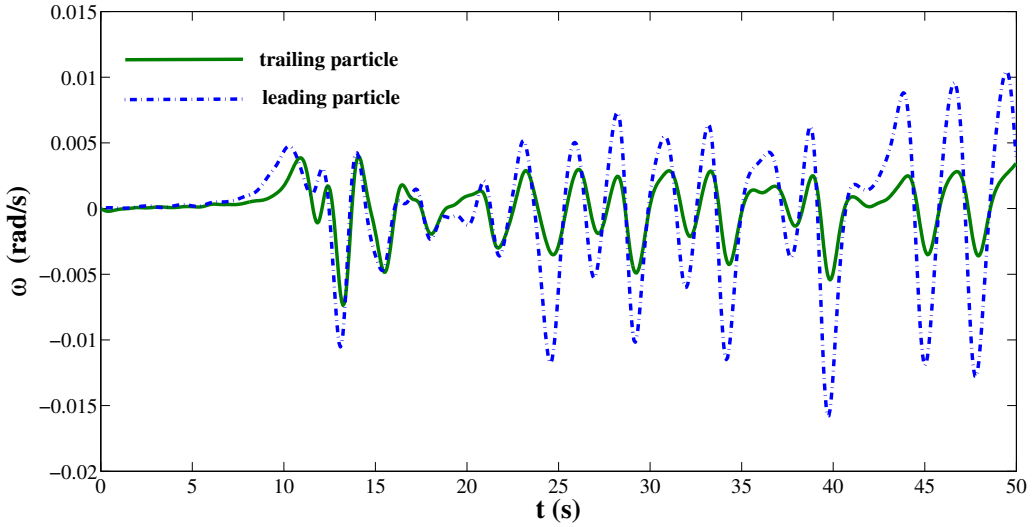

Figure 16: Settling dynamics of two particles initially aligned vertically, with parameters $W = 8D$ and $Re = 3$. (a) Vertical separation distance. (b) Angular velocity ω (positive = counter-clockwise rotation).

(a) Vertical separation distance

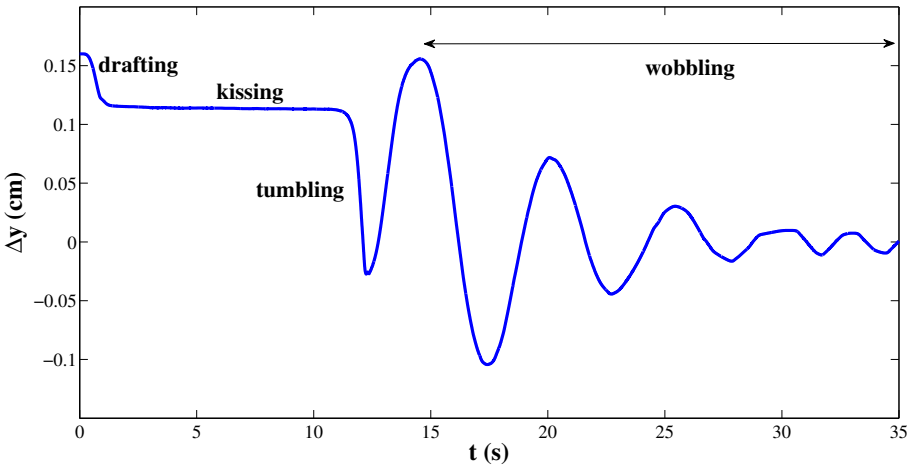

(b) Horizontal separation distance

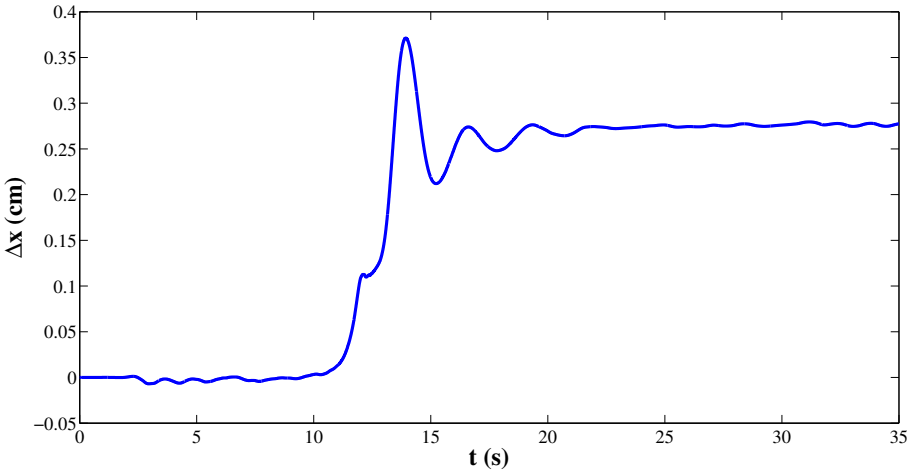

(c) Angular velocities

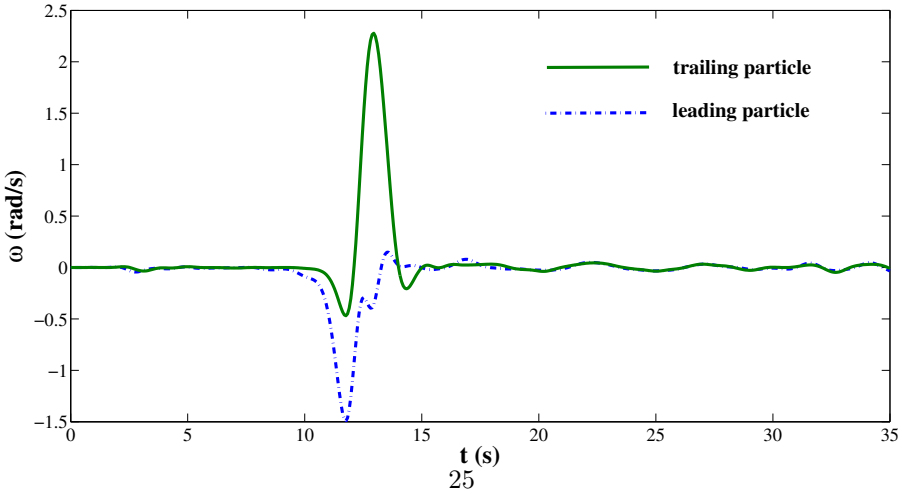

Figure 17: Settling dynamics of two particles at $Re = 14$ initially aligned vertically along the centerline in a channel of width $W = 8D$. (a) Vertical separation distance. (b) Horizontal separation distance. (c) Angular velocity ω (positive = counter-clockwise).

this time and find that after the second tumble, the particles separate vertically as they migrate toward the center of the channel. By time $t = 10$ s they settle at roughly the same speed and no longer interact in any significant way. Our computations also exhibit much the same qualitative behavior as the experiments reported in [17, 29] and numerical simulations from [19, 46].

5.2. Two vertically-aligned particles, released off-center.

In this section, we consider an asymmetric initial layout where the two particles are aligned vertically (again separated by a distance $2D$) but instead have their centers of mass displaced to the left of center at location $x = W/4$. This initial geometry is depicted in Figure 15(b).

Results are first reported for a channel of width $W = 4D$ and four values of Reynolds number: $Re = 1.5, 2$, 10 and 47. For the three smallest values of Reynolds number, we observe the behavior pictured in Figures 21 and 22. Initially, both particles drift toward the right, with the trailing particle moving toward the centerline while the leading particle moves to a point roughly mid-way between the centerline and the right wall. At the same time, the trailing particle speeds up in the wake of the leading particle so that they approach the same height. After this initial realignment, the two lowest Reynolds numbers ($Re = 1.5$, 2) undergo another slight adjustment in the horizontal locations so that the two particles are located symmetrically about the centerline; interestingly, the two particles in the $Re = 10$ case remain in a slightly asymmetric layout relative to the centerline. After that, the particles fall with roughly constant speed and without changing x-locations in the channel. The snapshots in Figure 22 for the $Re = 2$ case show that the particles do not enter either kissing or tumbling phases.

Both particles experience a distinct rotational motion as shown in Figure 23 for $Re = 2$, but the magnitude of the angular velocity is not as large as was observed during the tumbling phase for the simulations in the previous section. Corresponding results for a channel of width $W = 8D$ do not show any significant difference in qualitative behavior.

A very different behavior is observed for the highest value of Reynolds number ($Re = 47$) as seen in Figures 24 and 25. Up to time $t \approx 7$ s the dynamics are similar to the lower Re cases in that the particles migrate to the right with the leading particle approaching closest to the wall. However, at this time the particles separate horizontally and a marked back-and-forth oscillation appears that grows in magnitude between times $t \approx 7$ and 23 s, until the oscillating particles overlap with each other near the centerline. At $t \approx 23$ s, the particles undergo a strong interaction in which they swap horizontal locations and move to positions symmetrically opposite to each other on either side of the channel. At this stage, they have reached a steady state with roughly constant vertical velocity. The growing horizontal oscillations in the time interval $[7, 23]$ are accompanied by a synchronized rotation of both particles (in opposite directions) that grows rapidly and then also dies out after $t \approx 23$ s (refer to Figure 24(b)).

5.3. Two horizontally-aligned particles.

We next simulate the motion of two particles initially aligned horizontally in a channel of width $W = 8D$. We consider two sets of initial conditions pictured in Figures 15(c) and (d), first where the particles are located symmetrically with respect to the channel centerline, and the second an asymmetric arrangement that is shifted to the left.

Our main aim here is to determine to what extend our results are able to reproduce the finite element simulations of FHJ [16] using $W = 8D$ and $Re = 1.52$. They computed particle dynamics such as that pictured in Figure 26 that can be separated into three distinct phases:

i. a first phase that consists of a rapid re-adjustment up to time $t^* \approx 500$ (measured in dimensionless time units, with to $t^* = t\sqrt{g/D}$) during which the particles separate horizontally to locations that are equally-spaced from the left and right walls.
ii. a second phase where the particles maintain their horizontal positions and fall together with the same vertical speed until $t^* \approx 4000$.
iii. a third phase in which the particles shift together to the right into a new equilibrium state where the left-most particle oscillates about the centerline, while the right-most particle is much closer to the right wall and also oscillates side-to-side but with smaller amplitude.

(a) Vertical separation distance

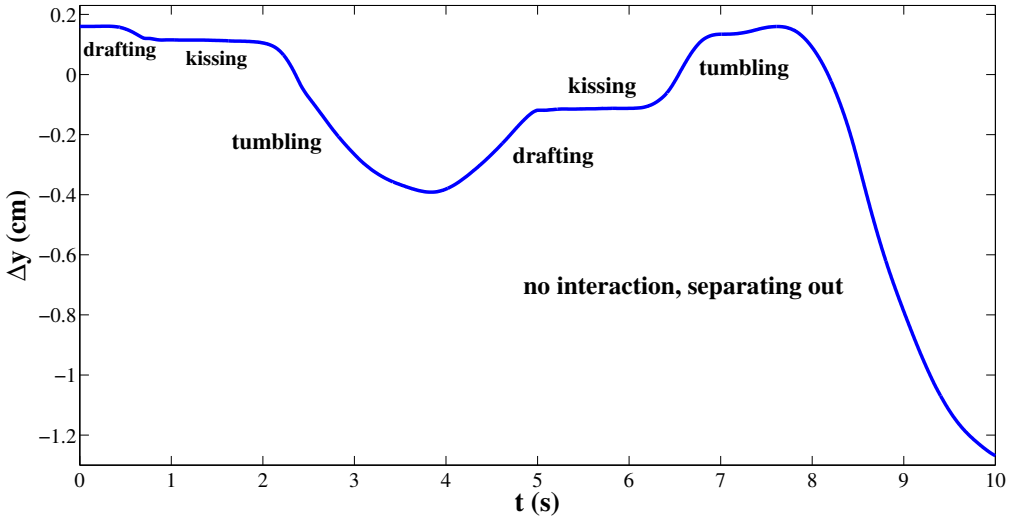

(b) Angular velocities

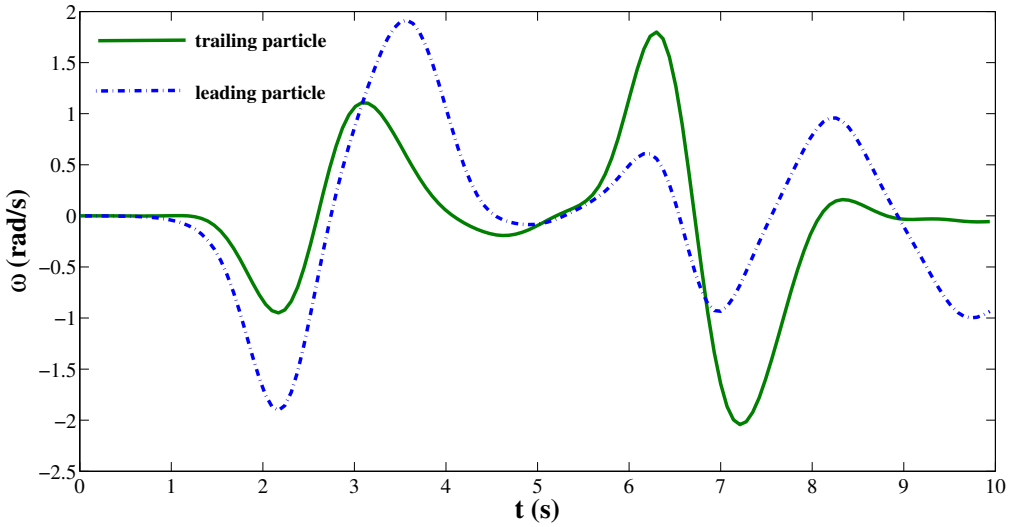

Figure 18: Settling dynamics of two particles at $Re = 80$ initially aligned vertically along the centerline in a channel of width $W = 8D$. (a) Vertical separation distance. (b) Angular velocity ω (positive = counter-clockwise).

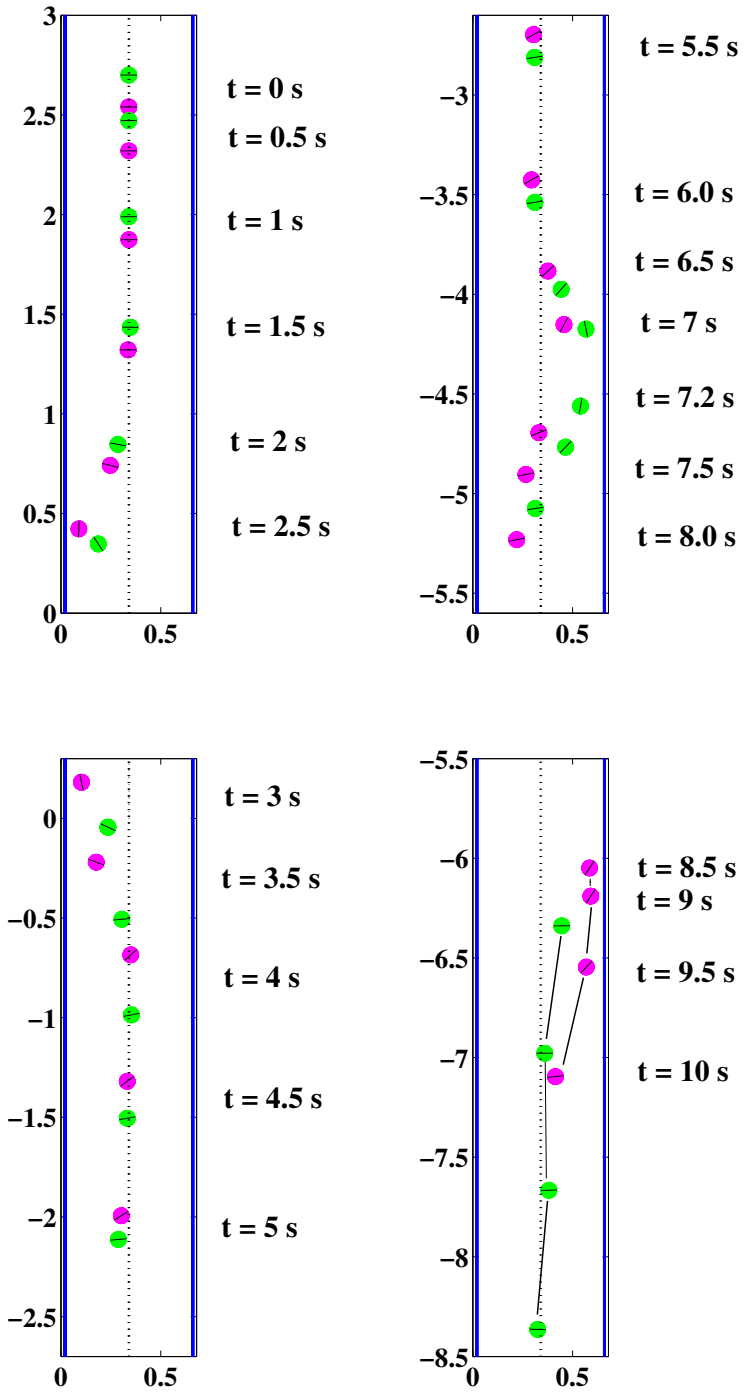

Figure 19: Snaphots of particle interactions in the channel of width $W = 8D$ with $Re = 80$, for the case when the particles are initially aligned vertically along the channel centerline.

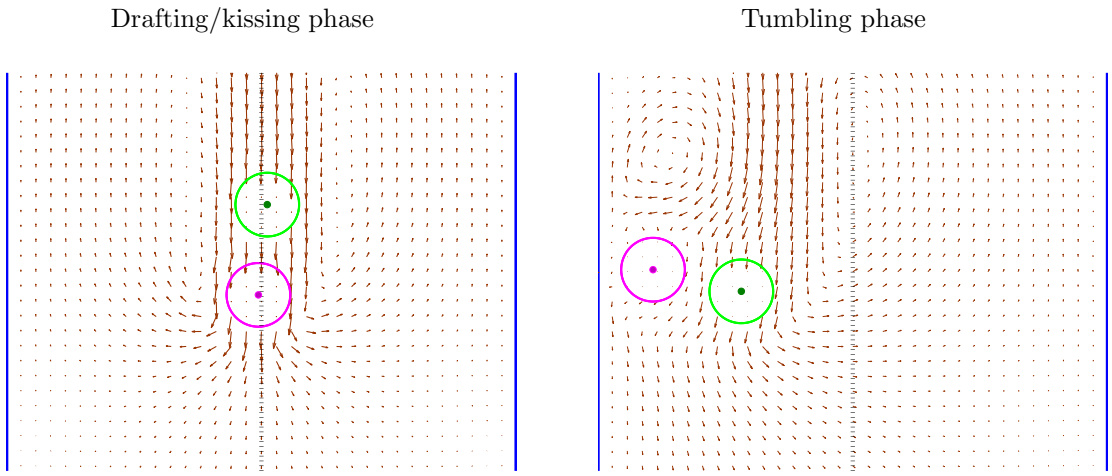

Figure 20: Velocity vector plots for the drafting/kissing (left) and tumbling phase (right) for the case when the particles are initially aligned vertically along the channel centerline. Parameters: $W = 8D$ and $Re = 80$.

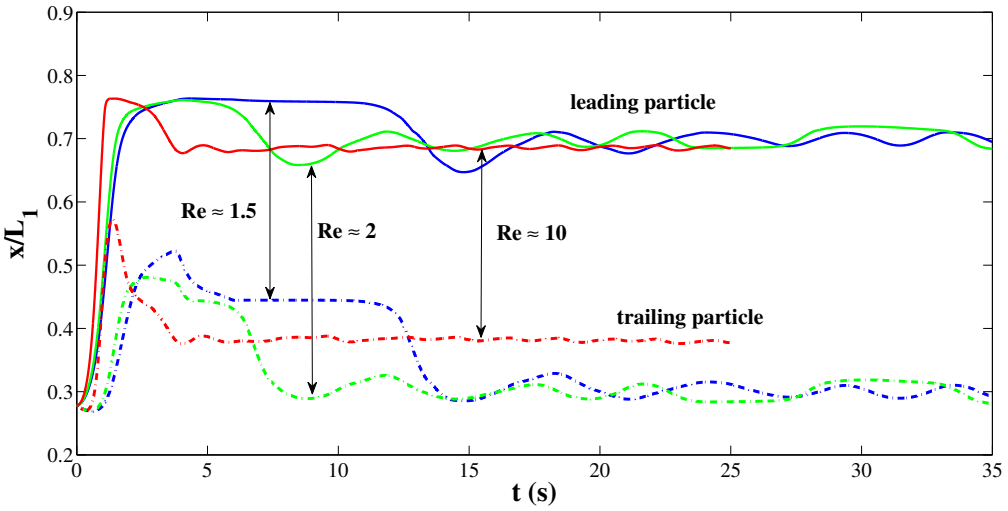

Figure 21: Horizontal particle locations for two particles initially aligned vertically but off-center. Parameter values: $W = 4D$ and $Re = 1.5$, 2, 10.

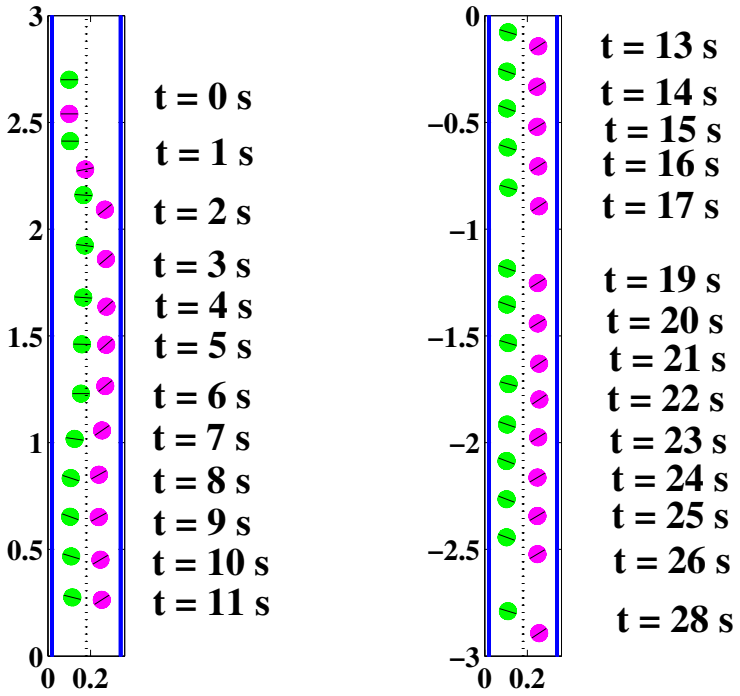

Figure 22: Snapshots of particle interactions for the case when the particles are initially aligned vertically, but off-center. Parameter values: $W = 4D$ and $Re = 2$.

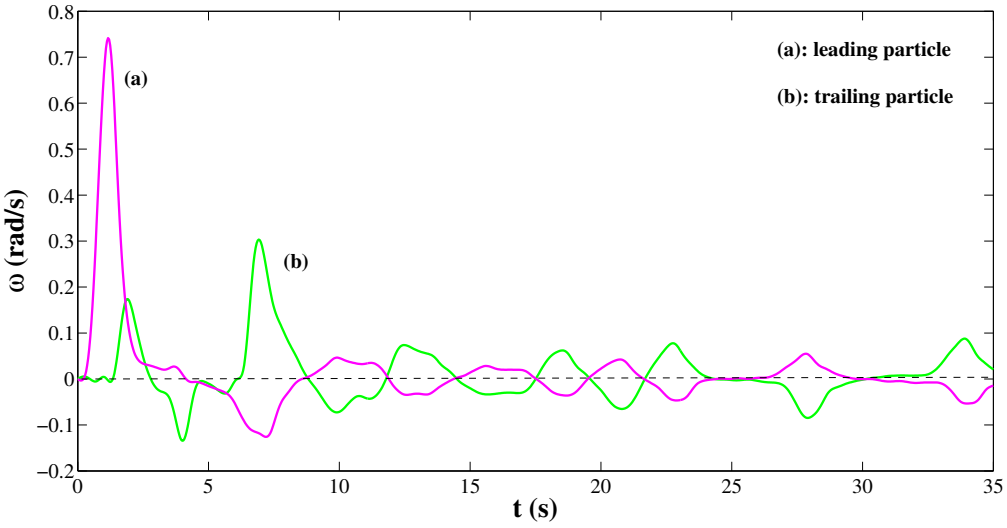

Figure 23: Angular velocity ω for two particles initially aligned vertically and off-center. Parameter values: $W = 4D$ and $Re = 2$.

(a) Horizontal positions

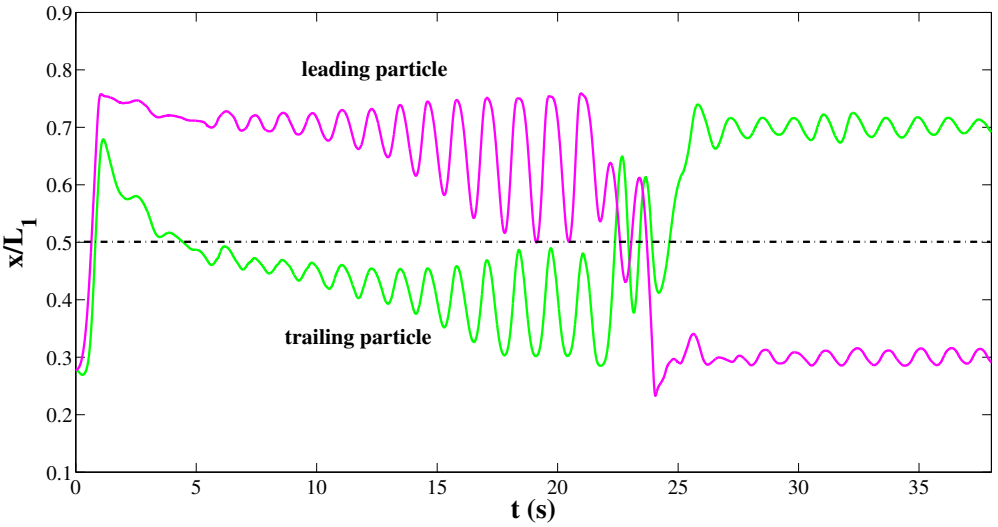

(b) Angular velocities

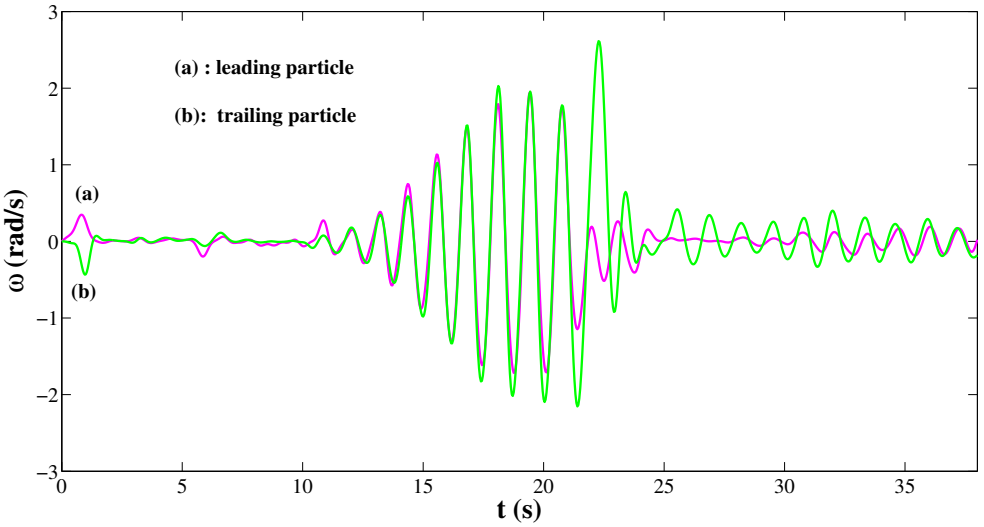

Figure 24: Settling dynamics of two particles initially aligned vertically and off-center, with parameters $W = 4D$ and $Re = 47$. (a) Horizontal positions. (b) Angular velocity ω (positive = counter-clockwise).

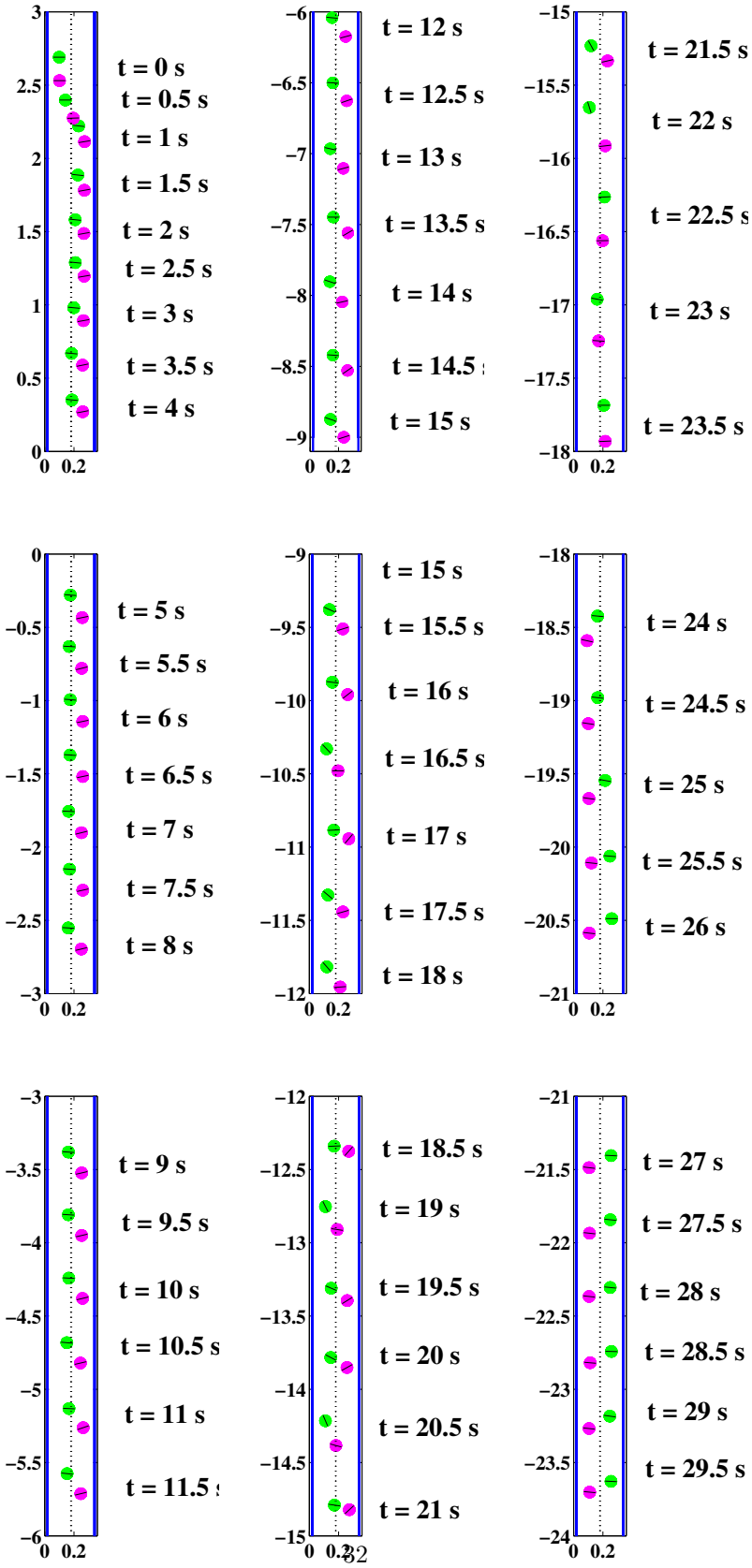

Figure 25: Snapshots of particle interactions for two particles initially aligned vertically, but off-center. Read from top to bottom, then left to right. Parameter values: $W = 4D$ and $Re = 47$.

We remark that FHJ's simulations were intended to reproduce the experiments of Jayaweera and Mason [28], wherein two long thin cylinders were settling in a large tank, with the same initial conditions and Re between 0.1 and 1.0. Jayaweera and Mason's discussion of their experimental results makes mention of the first two phases but not phase iii.

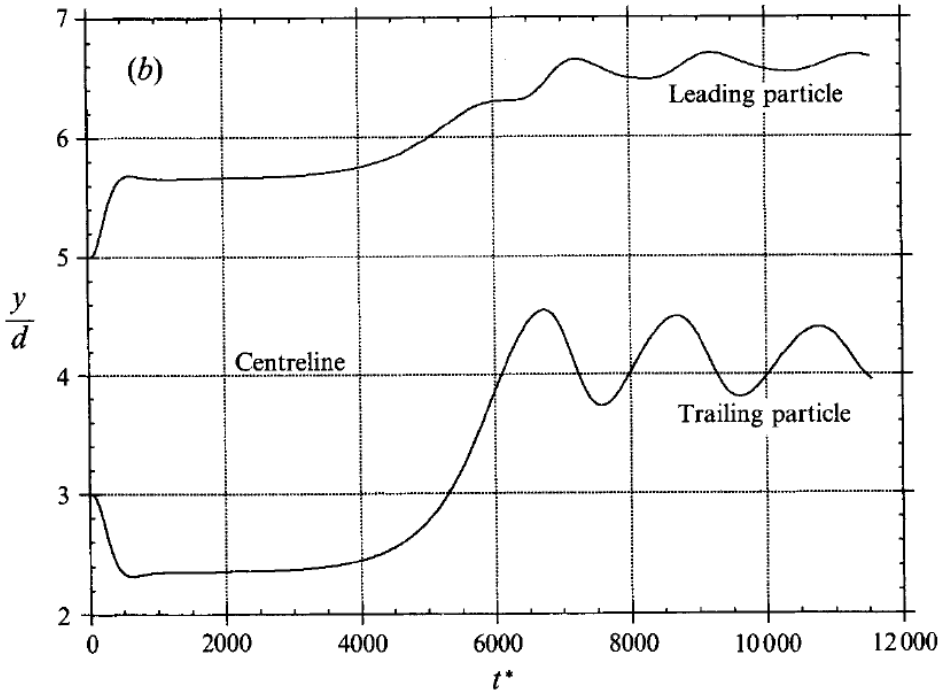

Figure 26: Horizontal locations of the two particles, as simulated by FHJ. Parameters: $W = 8D$, $Re = 1.52$. Reproduced from [16, Figure 32(b)], with permission.

We begin with the symmetric case where the two particles have initial horizontal positions

$$x = \frac{L_x}{2} - \frac{W}{8} \quad \text{and} \quad x = \frac{L_x}{2} + \frac{W}{8}, \tag{38}$$

and Reynolds number $Re = 1.6$ which is very close to FHJ's value. The horizontal locations of the simulated particles are pictured in Figure 27, with the plot axes rescaled to use the same dimensionless variables as FHJ in Figure 26. Our solution exhibits a steady state at long times that corresponds to positions $x/D \approx 2.25$ and 5.75 located symmetrically across the centerline; these positions are very close to those obtained in FHJ's phase ii. Furthermore, the rapid transient in phase i ends at a dimensionless time of roughly $t^* = 500$, which is also very close to FHJ's value. These two results suggest that our numerics are consistent with FHJ during phases i and ii and that we are capturing this portion of the motion properly.

However, we do not capture the same phase iii behavior since our two particles never deviate from their steady state locations for $t^* \gtrsim 4000$ when FHJ's phase iii begins. Similar dynamics to FHJ's phase iii have also been computed by Aidun and Ding [1] with a lattice-Boltzmann method, and they ascribe this periodic behavior to the appearance of a solution bifurcation. It is likely that this bifurcation is sensitive not only to solution parameters but also to the presence of numerical error. Therefore, we suspect that the first order accuracy of our IB method may be preventing the numerics from capturing this transition to a periodic state at longer times.

We repeated the previous calculation by increasing the Reynolds number to $Re = 4.4$ and our results are pictured in Figures 28 and 29 which exhibit similar dynamics to the lower Re case. In particular, we still observe no transition to phase iii behavior even at this higher Reynolds number. These results give us some

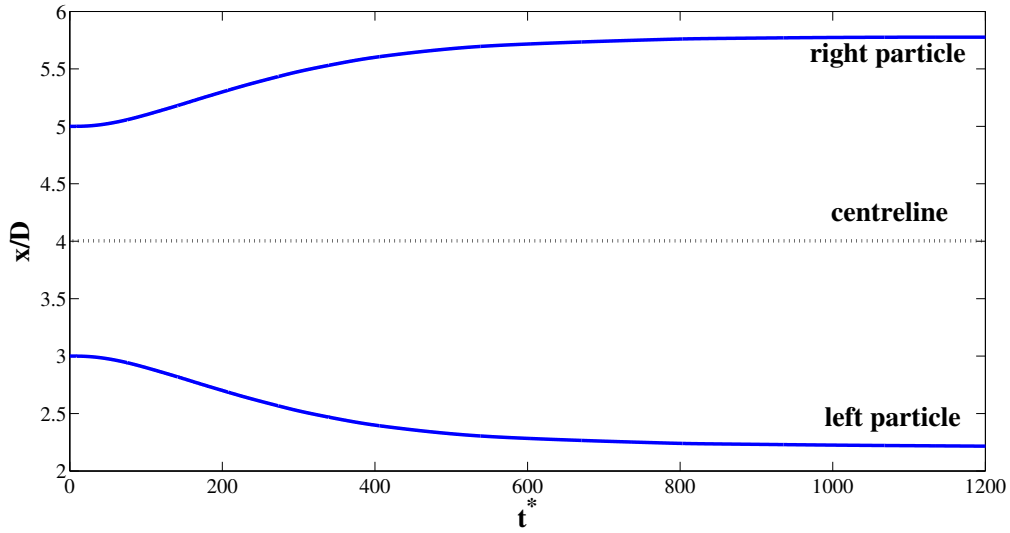

Figure 27: Horizontal particle positions for two particles initially located on the same horizontal line, and symmetric about the centerline. Parameter values: $W = 8D$ and $Re = 1.6$.

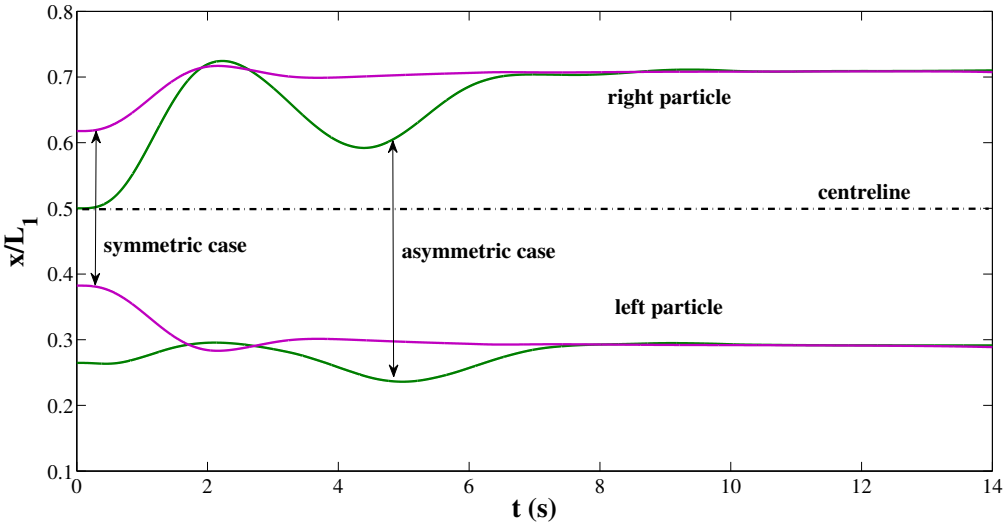

Figure 28: Horizontal particle positions for two particles initially located on the same horizontal line. Both symmetrical and asymmetric initial conditions are pictured. Parameter values: $W = 8D$ and $Re = 4.4$.

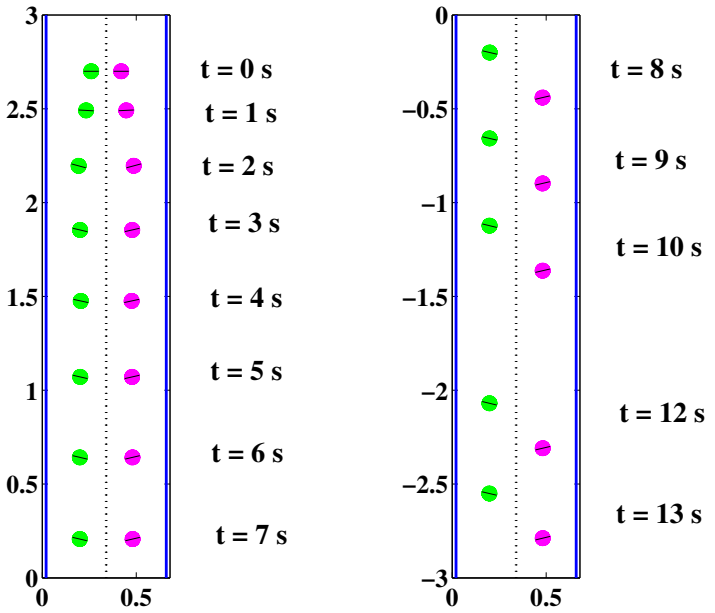

Figure 29: Snapshots of particle interactions for two particles initially aligned horizontally and centered. Parameter values: $W = 8D$ and $Re = 4.4$.

confidence that our IB simulations are reproducing physically-relevant behavior corresponding to phases i and ii, but a more detailed numerical study is required in order to determine the source of the discrepancy between our method and FHJ's approach.

The perfectly symmetric initial conditions used above are somewhat artificial, and will never actually occur in a real flow. Hence, we have also simulated an asymmetric initial placement of the particles given by

$$x = \frac{L_x}{2} - \frac{W}{4} \quad \text{and} \quad x = \frac{L_x}{2}, \tag{39}$$

in which the initial particle locations from (38) are shifted a distance $W/8$ to the left as pictured in Figure 15(d). Otherwise, the channel width $W = 8D$ and Reynolds number $Re = 4.4$ remain the same as in the symmetric case. The numerical results are shown in Figures 28 and 30, where the particles exhibit similar dynamics to the symmetric case and approach the same long-term equilibrium solution. The only difference can be seen in the transient motion where the particles undergo one additional oscillation in the horizontal locations en route to steady state.

6. Conclusions.

The main aim of this paper is to demonstrate the ability of the immersed boundary method to simulate realistic dynamics of solid particles settling under gravity within a Newtonian incompressible fluid. The solid particles are modelled as a network of stiff springs, while the added mass of the particles is incorporated using an extra gravitational forcing term that is spread onto fluid points via a regularized delta function. Numerical simulations of a single particle show good agreement with the most accurate empirical formula for wall-corrected settling velocity due to Faxén. Furthermore, two-particle simulations reproduce qualitatively features of the dynamics seen in both experiments and numerical simulations.

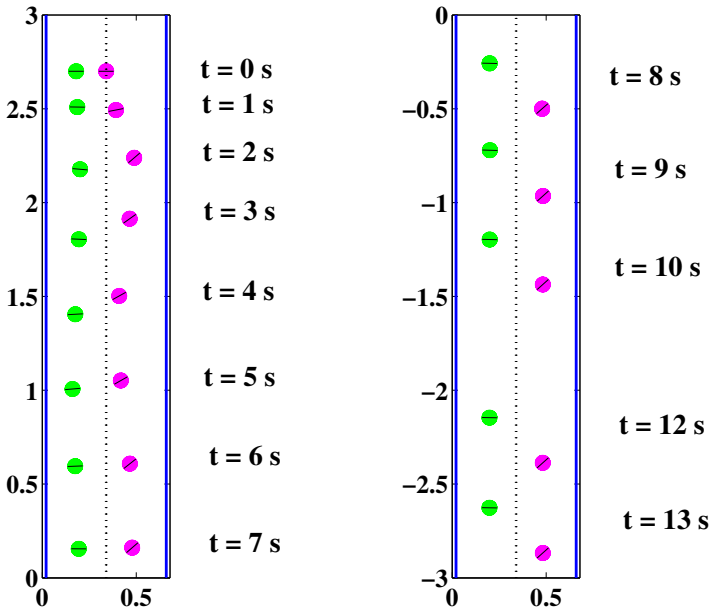

Figure 30: Snapshots of interactions for two particles initially aligned horizontally and off-center. Parameter values: $W = 8D$ and $Re = 4.4$.

This study is by no means a comprehensive comparison to other results from the extensive literature on particle sedimentation, but rather sets the stage for such a study in future. In particular, we plan to perform a more detailed comparison with other published results, focusing first on our idealized cylindrical particles. By implementing improvements to the numerical algorithm that increase accuracy of the solution approximation (such as in [31]) we hope to be able to explain the discrepancy we observed between our results and those of Feng, Hu and Joseph [16]. After that, the natural next step would be to extend our numerical method to 3D in order to permit simulations spherical particle interactions in a more realistic geometry.

We emphasize that this study is a "proof-of-concept" that the immersed boundary method may be applied to simulating the sedimentation of particles that are denser than the suspending fluid. We make no claim to improve on or to compete with other numerical methods that are specially-tailored to deal with rigid, non-deformable particles. Instead, our ultimate goal is to solve sedimentation problems involving irregularly-shaped and highly deformable particles, which to our knowledge has not been sufficiently well studied in the literature. Such particle systems arise in the study of suspensions of red blood cells, wood pulp fibers, vesicles, bubbles, etc. Making use of the uniform triangulated meshes from the DistMesh package will allow us to deal with more general particle shapes. Furthermore, we plan to take advantage of recent developments in massively parallel immersed boundary algorithms by Wiens and Stockie [51], which should prove instrumental in allowing efficient 2D and 3D immersed boundary simulations to be performed for non-dilute suspensions containing large numbers of particles.

References

[1] C. K. Aidun and E.-J. Ding. Dynamics of particle sedimentation in a vertical channel: Period-doubling bifurcation and chaotic state. *Phys. Fluids*, 15(6):1612–1621, 2003.

[2] E. Alpkvist and I. Klapper. Description of mechanical response including detachment using a novel particle model of biofilm/flow interaction. *Water Sci. Tech.*, 55:265–273, 2007.

[3] G. K. Batchelor. *An Introduction to Fluid Dynamics*. Cambridge University Press, 1967.

[4] A. Ben Richou, A. Ambari, M. Lebey, and J. K. Naciri. Drag force on a circular cylinder midway between two parallel plates at $Re < 1$. Part 2: moving uniformly (numerical and experimental). *Chem. Eng. Sci.*, 60(10):2535–2543, 2005.
[5] A. Ben Richou, A. Ambari, and J. K. Naciri. Drag force on a circular cylinder midway between two parallel plates at $Re < 1$. Part 1: Poiseuille flow (numerical). *Chem. Eng. Sci.*, 59(15):3215–3222, 2004.
[6] H. Brenner. Hydrodynamic resistance of particles at small Reynolds number. *Adv. Chem. Eng.*, 6:287–438, 1966.
[7] W.-P. Breugem. A second-order accurate immersed boundary method for fully resolved simulations of particle-laden flows. *J. Comput. Phys.*, 231(13):4469–4498, 2012.
[8] T. T. Bringley. *Analysis of the Immersed Boundary Method for Stokes Flow*. PhD thesis, Department of Mathematics, New York University, May 2008.
[9] R. Bürger and W. L. Wendland. Sedimentation and suspension flows: Historical perspective and some recent developments. *J. Eng. Math.*, 41:101–116, 2001.
[10] S. Champmartin and A. Ambari. Kinematics of a symmetrically confined cylindrical particle in a "Stokes-type" regime. *Phys. Fluids*, 19:073303, 2007.
[11] R. P. Chhabra, S. Agarwal, and K. Chaudhary. A note on wall effect on the terminal falling velocity of a sphere in quiescent Newtonian media in cylindrical tubes. *Powder Tech.*, 129:53–58, 2003.
[12] R. H. Davis and A. Acrivos. Sedimentation of noncolloidal particles at low Reynolds numbers. *Annu. Rev. Fluid Mech.*, 17:91–118, 1985.
[13] A. Dupuis, P. Chatelain, and P. Koumoutsakos. An immersed boundary-lattice-Boltzmann method for the simulation of the flow past an impulsively started cylinder. *J. Comput. Phys.*, 227(9):4486–4498, 2008.
[14] O. H. Faxén. Forces exerted on a rigid cylinder in a viscous fluid between two parallel fixed planes. *Proceedings of the Royal Swedish Academy of Sciences*, 187:1–13, 1946.
[15] R. D. Felice. The sedimentation velocity of dilute suspensions of nearly monosized spheres. *Int. J. Multiphase Flow*, 25:559–574, 1999.
[16] J. Feng, H. H. Hu, and D. D. Joseph. Direct simulation of initial value problems for the motion of solid bodies in a Newtonian fluid. Part 1. Sedimentation. *J. Fluid Mech.*, 261:95–134, 1994.
[17] A. F. Fortes, D. D. Joseph, and T. S. Lundgren. Nonlinear mechanics of fluidization of beds of spherical particles. *J. Fluid Mech.*, 177:467–483, 1987.
[18] S. Ghosh. *The immersed boundary method for simulating gravitational settling and fluid shear-induced deformation of elastic structures*. PhD thesis, Department of Mathematics, Simon Fraser University, Burnaby, Canada, Mar. 2013.
[19] R. Glowinski, T. W. Pan, T. I. Hesla, D. D. Joseph, and J. Périaux. A fictitious domain approach to the direct numerical simulation of incompressible viscous flow past moving rigid bodies: Application to particulate flow. *J. Comput. Phys.*, 169(2):363–426, 2001.
[20] B. E. Griffith, R. D. Hornung, D. M. McQueen, and C. S. Peskin. An adaptive, formally second order accurate version of the immersed boundary method. *J. Comput. Phys.*, 223(1):10–49, 2007.
[21] É. Guazzelli and J. F. Morris. *A Physical Introduction to Suspension Dynamics*. Cambridge Texts in Applied Mathematics. Cambridge University Press, 2012.
[22] S. Haeri and J. S. Shrimpton. On the application of immersed boundary, fictitious domain and body-conformal mesh methods to many particle multiphase flows. *Int. J. Multiphase Flow*, 40:38–55, 2012.
[23] J. Happel and H. Brenner. *Low Reynolds number hydrodynamics, with special applications to particulate media*. Mechanics of fluids and transport processes. Martinus Nijhoff Publishers, 1983.
[24] J. P. Hernández-Ortiz. *Boundary Integral Equations for Viscous Flows – non-Newtonian Behavior and Solid Inclusions*. PhD thesis, University of Wisconsin-Madison, Department of Mechanical Engineering, 2004.
[25] M. M. Hopkins and L. J. Fauci. A computational model of the collective fluid dynamics of motile microorganisms. *J. Fluid Mech.*, 455:149–174, 2002.
[26] H. H. Hu. Direct simulation of flows of solid-liquid mixtures. *Int. J. Multiphase Flow*, 22(2):335–352, 1996.
[27] H. H. Hu, D. D. Joseph, and A. F. Fortes. Experiments and direct simulation of fluid particle motions. *Int. Vid. J. Eng. Res.*, 2:17–24, 1997.
[28] K. O. L. F. Jayaweera and B. J. Mason. The behaviour of freely falling cylinders and cones in a viscous fluid. *J. Fluid Mech.*, 22(4):709–720, 1965.
[29] D. D. Joseph, A. Fortes, T. S. Lundgren, and P. Singh. Nonlinear mechanics of fluidization of spheres, cylinders and disks in water. In *Advances in Multiphase Flow and Related Problems*, pages 101–122. SIAM, Philadelphia, PA, 1987.
[30] A. J. C. Ladd. Numerical simulations of particulate suspensions via a discretized Boltzmann equation. Part II. Numerical results. *J. Fluid Mech.*, 271:311–339, 1994.
[31] M.-C. Lai and C. S. Peskin. An immersed boundary method with formal second-order accuracy and reduced numerical viscosity. *J. Comput. Phys.*, 160(2):705–719, 2000.
[32] R. Mittal and G. Iaccarino. Immersed boundary methods. *Annu. Rev. Fluid Mech.*, 37:239–261, 2005.
[33] R. Münster, O. Mierka, and S. Turek. Finite element-fictitious boundary methods (FEM-FBM) for 3D particulate flow. *Int. J. Numer. Meth. Fluids*, 69(2):294–313, 2012.
[34] P. O. Persson and G. Strang. A simple mesh generator in MATLAB. *SIAM Review*, 46(2):329–345, 2004.
[35] C. S. Peskin. The immersed boundary method. *Acta Numer.*, 11:1–39, 2002.
[36] N. Phan-Thien and X.-J. Fan. Viscoelastic mobility problem using a boundary element method. *J. Non-Newton. Fluid Mech.*, 105(2-3):131–152, 2002.
[37] G. Pianet and E. Arquis. Simulation of particles in fluid: a two-dimensional benchmark for a cylinder settling in a wall-bounded box. *Euro. J. Mech. B Fluids*, 27:309–321, 2008.
[38] A. Prosperetti and G. Tryggvason. *Computational Methods for Multiphase Flow*. Cambridge University Press, 2007.

[39] D. Qi. Lattice-Boltzmann simulations of particles in non-zero-Reynolds-number flows. *J. Fluid Mech.*, 385:41–62, 1999.
[40] J. F. Richardson and W. N. Zaki. Sedimentation and fluidisation: Part I. *Trans. Inst. Chem. Eng.*, 32:35–53, 1954.
[41] J. M. Stockie. *Analysis and Computation of Immersed Boundaries, with Application to Pulp Fibres*. PhD thesis, Institute of Applied Mathematics, University of British Columbia, Vancouver, Canada, 1997.
[42] J. M. Stockie. Modelling and simulation of porous immersed boundaries. *Comput. Struct.*, 87(11-12):701–709, 2009.
[43] G. G. Stokes. Section IV. Determination of the motion of a fluid about a sphere which moves uniformly with a small velocity. In *Mathematical and Physical Papers*, volume III of *The Sources of Science, No. 33*, pages 55–67. Cambridge University Press, Teddington, UK, second edition, 1966. First published in 1901.
[44] D. Sucker and H. Brauer. Fluiddynamik bei quer angeströmten Zylindern. *Heat Mass Transfer*, 8(3):149–158, 1975.
[45] Y. Takaisi. The drag on a circular cylinder moving with low speeds in a viscous liquid between two parallel walls. *J. Phys. Soc. Japan*, 10:685–693, 1955.
[46] M. Uhlmann. An immersed boundary method with direct forcing for the simulation of particulate flows. *J. Comput. Phys.*, 209:448–476, 2005.
[47] P. Vasseur and R. G. Cox. The lateral migration of spherical particles sedimenting in a stagnant bounded fluid. *J. Fluid Mech.*, 80(3):561–591, 1977.
[48] J. Wang and A. Layton. Numerical simulations of fiber sedimentation in Navier-Stokes flow. *Commun. Comput. Phys.*, 5(1):61–83, 2009.
[49] Z. Wang, J. Fan, and K. Luo. Combined multi-direct forcing and immersed boundary method for simulating flows with moving particles. *Int. J. Multiphase Flow*, 34:283–302, 2008.
[50] C. M. White. The drag of cylinders in fluids at slow speeds. *Proc. Roy. Soc. A*, 186:472–479, 1946.
[51] J. K. Wiens and J. M. Stockie. Massively parallelized immersed boundary method. In preparation.
[52] L. Zhu and C. S. Peskin. Simulation of a flapping flexible filament in a flowing soap film by the immersed boundary method. *J. Comput. Phys.*, 179(2):452–468, 2002.
[53] T. Zisis and E. Mitsoulis. Viscoplastic flow around a cylinder kept between parallel plates. *J. Non-Newton. Fluid Mech.*, 105:1–20, 2002.